Bohn, N., Guanter, L., Kuester, T., Preusker, R., Segl, K. (2020): Coupled retrieval of the three phases of water from spaceborne imaging spectroscopy measurements. - Remote Sensing of Environment, 242, 111708.

https://doi.org/10.1016/j.rse.2020.111708

# Coupled retrieval of the three phases of water from spaceborne imaging spectroscopy measurements

Niklas Bohn[a,*], Luis Guanter[a,b], Theres Kuester[a], René Preusker[c], Karl Segl[a]

[a] *GFZ German Research Centre for Geosciences, Remote Sensing and Geoinformatics, Telegrafenberg, 14473 Potsdam, Germany*
[b] *Centro de Tecnologías Físicas, Universitat Politècnica de València, Camí de Vera s/n, 46022 Valencia, Spain*
[c] *Freie Universitaet Berlin, Department of Earth Sciences, Institute for Space Sciences, Carl-Heinrich-Becker-Weg 6-10, 12165 Berlin, Germany*

**Abstract**

Measurements of reflected solar radiation by imaging spectrometers can quantify water in different states (solid, liquid, gas) thanks to the discriminative absorption shapes. We developed a retrieval method to quantify the amount of water in each of the three states from spaceborne imaging spectroscopy data, such as those from the German EnMAP mission. The retrieval couples atmospheric radiative transfer simulations from the MODTRAN5 radiative transfer code to a surface reflectance model based on the Beer-Lambert law. The model is inverted on a per-pixel basis using a maximum likelihood estimation formalism. Based on a unique coupling of the canopy reflectance model HySimCaR and the EnMAP end-to-end simulation tool EeteS, we performed a sensitivity analysis by comparing the retrieved values with the simulation input leading to an $R^2$ of 0.991 for water vapor and 0.965 for liquid water. Furthermore, we applied the algorithm to airborne AVIRIS-C data to demonstrate the ability to map snow/ice extent as well as to a CHRIS-PROBA dataset for which concurrent field measurements of canopy water content were available. The comparison between the retrievals and the ground measurements showed an overall $R^2$ of 0.80 for multiple crop types and a remarkable clustering in the regression analysis indicating a dependency of the retrieved water content from the physical structure of the vegetation. In addition, the algorithm is able to produce smoother and more physically-plausible water vapor maps than the ones from the band ratio approaches used for multispectral data, since biases due to background reflectance are reduced. The demonstrated potential of imaging spectroscopy to provide accurate quantitative measures of water from space will be further exploited using upcoming spaceborne imaging spectroscopy missions like PRISMA or EnMAP.

*Keywords:* Imaging spectroscopy, Atmospheric correction, Water vapor, Canopy water content, EnMAP

## 1. Introduction

Imaging spectroscopy or hyperspectral remote sensing of the Earth's system is based on spectroscopic measurements of the solar radiation reflected by atmospheric and surface components in contiguous spectral channels (Goetz et al., 1985; Vane and Goetz, 1988). They cover the visible (VIS), near-infrared (NIR) and shortwave-infrared (SWIR) part of the solar spectrum featuring a wavelength range from 400 nm to 2500 nm (Goetz et al., 1985). Since land, water and atmosphere constituents show characteristic spectral signatures, spectroscopic measurements enable their identification and quantification using physically-based retrievals by modeling atmospheric and surface absorption features. Based on this technique, imaging spectroscopy can be applied to a wide range of different scientific disciplines in Earth Observation (EO) such as quantification of atmospheric greenhouse gases and aerosols, monitoring vegetation phenology, soil and mineral mapping, as well as retrieval of water constituents over inland water bodies, coastal areas and open ocean (Schaepman et al., 2009). Imaging spectroscopy can therefore substantially contribute to a better understanding of Earth's ecosystems and support studies of climate change (Thompson et al., 2015).

So far, research in imaging spectroscopy has been mostly based on airborne spectrometers and simulations of spaceborne technology, but a number of satellite missions were recently launched, or are to be launched soon. The German DLR Earth Sensing Imaging Spectrometer (DESIS) (Mueller et al., 2016) and the Italian Hyperspectral Precursor of the Application Mission (PRISMA) (Loizzo et al., 2018) came into operation in June, 2018 and March, 2019, respectively. The German Environmental Mapping and Analysis Program (EnMAP) (Guanter et al., 2015) is scheduled for launch in 2021 and further missions like the NASA Surface Biology and Geology (SBG) (Lee et al., 2015) and the Copernicus Hyperspectral Imaging Mission (CHIME) (Bach et al., 2018) led by ESA are in the planning phase.

The remote sensing of the three phases of water is an ideal example of the potential of imaging spectroscopy for environmental sciences, since it makes it possible to identify and quantify water in different states due to the presence of sufficient narrow bands in the NIR (Green et al., 2006). In this connection, the use of spaceborne imaging spectroscopy measurements pre-

*Corresponding author at: GFZ German Research Centre for Geosciences, Remote Sensing and Geoinformatics, Telegrafenberg, 14473 Potsdam, Germany. Tel.: +49 331 288 28969.

*Email address:* nbohn@gfz-potsdam.de (Niklas Bohn)

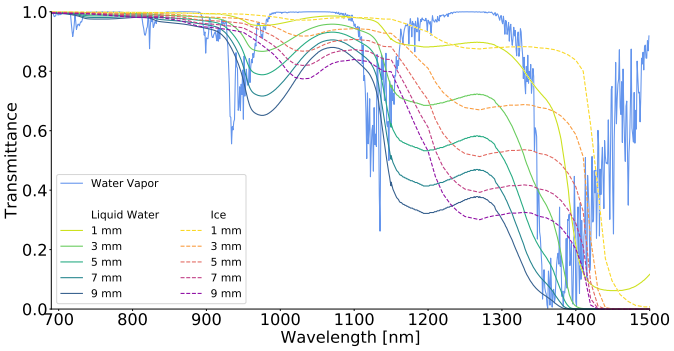


Figure 1: Overlapping transmittance spectra of the three phases of water. The line of water vapor is calculated for an absorption of 5 mm precipitable water. The lines of liquid water and ice are shown for five different absorption path lengths between 1 mm and 9 mm.

sented in our study enables new possibilities in mapping local and global trends of water vapor, liquid water and ice. On one hand, it significantly contributes to climate research (Diedrich et al., 2013). On the other, it is essential for evaluating the water use efficiency of plants and their physiological status and health (see Clevers et al. (2010); Wocher et al. (2018)). Finally, it helps to assess the distribution and availability of fresh water through predicting snow melt rates and processes (Green et al., 2006).

Green et al. (2006) introduced a method to simultaneously estimate the path lengths of water vapor, liquid water and ice from airborne imaging spectroscopy data by applying a physically-based nonlinear least squares inversion of the MODTRAN Radiative Transfer Model (RTM) (Berk et al., 1989) linked to a surface reflectance model. The latter incorporates the Beer-Lambert law, which expresses the radiation absorption as a function of the path length of pure liquid water and ice (Born and Wolf, 1959). While water vapor can be inferred from the MODTRAN simulations, the surface reflectance model enables the retrieval of the other two phases. The approach is based on the decoupling of the overlapping absorption lines of water vapor, liquid water and ice (Green et al., 2006; Thompson et al., 2015) (Figure 1). The lines of liquid water and ice are shifted towards longer wavelengths. This displacement, in combination with moderate absorption energies enables a spectroscopic separation of the three phases (Green et al., 2006). The study of Green et al. (2006) can be seen as the first assessment to infer the amounts of all three phases of water in a coupled way. Earlier studies only present combined vapor and liquid retrievals (Gao and Goetz, 1990; Green et al., 1991; Gao, 1996). Thompson et al. (2015) modified the method of Green et al. (2006) by a linear approximation of the inversion procedure, and additionally present an application on measuring cloud thermodynamic phase (Thompson et al., 2016). Each of the aforementioned retrieval studies used data from the airborne AVIRIS-C instrument (see Green et al. (1998); Vane et al. (1993)).

In view of the upcoming satellite missions, this work presents a novel application of the existing coupled retrieval of the three phases of water by extending the approach to spaceborne imaging spectroscopy measurements. We evaluate the performance of the algorithm through a sensitivity analysis based on simulated EnMAP data, which is new compared with previous applications, and show retrieval uncertainties, and discuss potential issues. Additionally, we test the algorithm on AVIRIS-C data to demonstrate the ability to map snow and ice extents, and use CHRIS-PROBA data as a proxy for future satellite measurements to illustrate the accuracy improvements using the three phases approach compared with band ratio water vapor retrievals. Finally, we focus on canopy water content (CWC) as a sort of liquid water because of its especial relevance to vegetation studies, and show the potential of the algorithm to quantitatively map CWC from space. This is done by comparing the retrievals with ground-based measurements and by discussing the interpretation of the derived top-of-canopy (TOC) values as a function of canopy structural parameters.

## 2. Methods

The coupled retrieval of the three phases of water is based on the inversion of a forward model, which models the top-of-atmosphere (TOA) radiance spectra. Applying this technique, the values of columnar water vapor (CWV), liquid water and ice can be inferred by minimizing the difference between modeled and measured spectra. The minimization uses a predefined cost function in an iterative optimization procedure.

### *2.1. Forward model*

Many algorithms in the field of remote sensing aim to infer specified quantities from a set of measurements, generally TOA radiance, by the inversion of a well-parameterized forward model. In a general form, the TOA radiance $\mathbf{y}$ is modeled by:

$$\mathbf{y} = \mathbf{F}(\mathbf{x}, \mathbf{b}) + \epsilon, \tag{1}$$

where $\mathbf{F}$ is the forward model, in this work composed of an atmospheric RTM and a surface reflectance model; $\mathbf{x}$ is the state vector, here containing CWV, liquid water and ice path lengths as well as slope and offset of the linear surface reflectance continuum of the chosen water absorption feature; $\mathbf{b}$ is the model parameter vector containing known parameters required by the forward model; and $\epsilon$ is an error vector containing different uncertainty components. In our case, the forward model input on one hand requires the observation geometry, i.e., the viewing zenith angle (VZA), the solar zenith angle (SZA), the relative azimuth angle (RAA) and the sensor altitude, and on the other hand, two physical parameters, namely the surface elevation (HSF) and aerosol optical thickness (AOT). $\epsilon$ consists of measurement errors caused by instrument calibration and noise, forward model errors, and errors in the state vector variables as well as the known model parameters.

#### *2.1.1. Atmospheric model*

For the atmospheric radiative transfer simulations we use the MODTRAN code (Berk et al., 1989, 2003; Bernstein et al., 2007). It is a 1D scalar RTM to calculate transmittance, radiance and fluxes for the ultraviolet (UV), VIS, NIR, SWIR and

Table 1: Gridding of LUT parameters for MODTRAN radiative transfer simulations (according to Guanter et al. (2009)).

| | 1 | 2 | 3 | 4 | 5 | 6 | 7 |
|---|---|---|---|---|---|---|---|
| VZA (°) | 0 | 10 | 20 | 30 | 40 | - | - |
| SZA (°) | 0 | 10 | 20 | 35 | 50 | 70 | - |
| RAA (°) | 0 | 25 | 50 | 85 | 120 | 155 | 180 |
| HSF (km) | 0 | 0.7 | 2.5 | 8 | - | - | - |
| AOT | 0.05 | 0.12 | 0.2 | 0.3 | 0.4 | 0.8 | - |
| CWV ($gcm^{-2}$) | 0 | 1 | 1.5 | 2 | 2.7 | 3.5 | 5 |

thermal infrared (TIR) spectrum covering a wavelength range of 0.2 - $10^4$ $\mu$m. We simulated wavelengths from 400 nm to 2500 nm to match the spectral coverage of EnMAP, AVIRIS-C and CHRIS-PROBA and executed MODTRAN in band model mode with a spectral sampling interval (SSI) of 1.0 $cm^{-1}$. The molecular absorption lines were obtained from the HITRAN database (Rothman et al., 2009), and multiple scattering was calculated using the DISORT N-stream (Stamnes et al., 1988).

Assuming clear sky and a plane-parallel atmosphere as well as a Lambertian surface, the TOA radiance $L_{TOA}$ can be modeled by a simplified solution of the radiative transfer equation following the approach of Chandrasekhar (1960):

$$L_{TOA} = L_0 + \frac{1}{\pi} * \frac{\rho_s(E_{dir}\mu_{sun} + E_{dif})T \uparrow}{1 - S\rho_s}, \tag{2}$$

where $L_0$ is the atmospheric path radiance; $\rho_s$ is the surface reflectance; $E_{dir}$ and $E_{dif}$ are the direct and diffuse solar irradiance, respectively, arriving at the surface; $\mu_{sun}$ is the cosine of the solar zenith angle; $T \uparrow$ is the total upward atmospheric transmittance; and $S$ is the spherical albedo of the atmosphere. All components except $\rho_s$ are functions of the state vector $\mathbf{x}$ and the model parameter vector $\mathbf{b}$ and are derived from the MODTRAN output by applying specific conversions following Guanter et al. (2009). To decrease the computational burden and to increase the processing speed, the atmospheric components were previously calculated for different atmospheric cases and stored in a multidimensional Look-Up-Table (LUT) (Table 1). The simulations sum up to 35,380 cases and are assumed to cover most of the acquisition conditions of the data used in this study.

#### 2.1.2. Surface reflectance model

Since water vapor is the only water phase appearing directly within the MODTRAN code, the atmospheric RTM has to be linked with a well-parameterized surface reflectance model to account for the path lengths of liquid water and ice. Whereas vapor is most dominant in the atmosphere, liquid and solid water can be classified as surface parameters. We use the method of Green et al. (2006) and model the surface reflectance as a linear change in reflectance with wavelength attenuated by the spectrally dependent absorption for liquid water and ice based on the Beer-Lambert law (Born and Wolf, 1959). Consequentially, the wavelength dependent surface reflectance $\rho_{s,\lambda}$ is expressed by:

$$\rho_{s,\lambda} = (a + b\lambda)e^{(-d_w\alpha_{w,\lambda} - d_i\alpha_{i,\lambda})}, \tag{3}$$

where $a$ and $b$ are offset and slope of the linear reflectance continuum; $\alpha_w$ and $\alpha_i$ are the wavelength dependent absorption coefficients of liquid water and ice, respectively; and $d_w$ and $d_i$ are the liquid water and ice path lengths, respectively, expressed in the same unit as wavelength. $\alpha_w$ and $\alpha_i$ are calculated by using the imaginary part of the complex index of refraction $k$, which is also wavelength dependent (Petty, 2004):

$$\alpha_\lambda = \frac{4\pi k_\lambda}{\lambda}. \tag{4}$$

To obtain $k$, we use the table of Kedenburg et al. (2012) for liquid water and the values from Warren (1984) for ice.

### 2.2. Inverse method

During the inversion of the forward model $\mathbf{F}$, water vapor, liquid water, and ice path lengths are iteratively adjusted to match modeled and measured spectra within the water absorption feature around 1140 nm. We chose the 1140 nm window since EnMAP features two overlapping detectors around the 940 nm water absorption band so that a complete coverage of the window using only one detector is not possible. Furthermore, both water bands can be used in a uniform manner to retrieve the amounts of the three phases (Thompson et al., 2015). The matching of the spectra is evaluated by a predefined cost function and the needed atmospheric parameters are obtained by a multidimensional linear interpolation within the LUT. Since we do not revert to prior or background knowledge about the uncertainties of the retrieval quantities, we apply a maximum likelihood estimation instead of optimal estimation to the iteration procedure with a focus on retrieval accuracy and processing speed. The mathematical expressions presented in the following section can be found in Rodgers (2000) as well as in applications by Diedrich et al. (2013) and Diedrich (2016).

#### 2.2.1. Maximum likelihood estimation

The maximum likelihood estimation enables the possibility to incorporate the error vector $\epsilon$ from Eq. 1 in terms of a measurement error covariance matrix $\mathbf{S}_e$ and to calculate the retrieval uncertainty for each state vector parameter as a by-product. The method is based on Bayes' theorem about probability density and takes Gaussian distribution of the errors as a basis. We invert the forward model by iteratively minimizing the cost function $f(\mathbf{x})$, which is commonly used for maximum likelihood and optimal estimation procedures:

$$\begin{aligned} f(\mathbf{x}) = (\mathbf{x} - \mathbf{x_a})^T \mathbf{S}_a^{-1} (\mathbf{x} - \mathbf{x_a}) \\ + (\mathbf{y} - \mathbf{F}(\mathbf{x}))^T \mathbf{S}_e^{-1} (\mathbf{y} - \mathbf{F}(\mathbf{x})), \end{aligned} \tag{5}$$

where $\mathbf{x_a}$ is the a priori state vector; and $\mathbf{S}_a$ is its error covariance matrix. Here, the difference between modeled spectra $\mathbf{F}(\mathbf{x})$ and measured spectra $\mathbf{y}$ is evaluated by taking into account the residuals between state vector and a priori state vector. Both quantities are weighted by their uncertainties and the state vector is changed at each iteration step to find the solution with the highest probability based on a given measurement and a priori information about the state. Since we apply the maximum likelihood estimation without considering information about the

uncertainties of the entries of $\mathbf{x_a}$, we fill the matrix $\mathbf{S}_a$ with sufficient high values (see Section 2.2.2). For convergence, we use the criterion:

$$(\mathbf{x}_i - \mathbf{x}_{i+1})^T \mathbf{S}_x^{-1} (\mathbf{x}_i - \mathbf{x}_{i+1}) < \epsilon_x n, \tag{6}$$

where $\mathbf{S}_x$ is the a posteriori or retrieval error covariance matrix; $\epsilon_x$ is a threshold in fraction of variance (here: $\epsilon_x = 0.01$); and $n$ is the number of dimensions of the state vector. The retrieval error covariance matrix gives a direct measure of the uncertainty of each parameter and is calculated by propagating the measurement uncertainty into the state vector space:

$$\mathbf{S}_x = (\mathbf{S}_a^{-1} + \mathbf{K}_i^T \mathbf{S}_e^{-1} \mathbf{K}_i)^{-1}, \tag{7}$$

where $\mathbf{K}$ is the Jacobian of the forward model and expresses the change in modeled TOA radiance in the $j$-th instrument channel for a small change in the $k$-th parameter of the solution state vector $\mathbf{x}$ at iteration step $i$:

$$\mathbf{K}_{j,k} = \{\frac{\delta y_j}{\delta x_k}\}. \tag{8}$$

$\mathbf{S}_e$ is decomposed into a matrix $\mathbf{S}_y$ describing the uncertainties due to physical instrument noise and a matrix $\mathbf{S}_b$ accounting for errors caused by unknown forward model parameters. $\mathbf{S}_y$ is calculated by:

$$\mathbf{S}_{j,k}^y = \{c_{j,k} \sigma_{y,j} \sigma_{y,k}\}, \tag{9}$$

where $\sigma_{y,j}$ is the measurement error in units of standard deviation for the $j$-th band of the imaging spectrometer; and $c_{j,k}$ is the correlation between the errors in the $j$-th and $k$-th band. For standard imaging spectrometers it can be assumed that $c_{j,k} = 0$. Consequentially, $\mathbf{S}_e$ has only diagonal elements:

$$(\delta_{j,j}^y)^2 = (\frac{L_j}{SNR_j})^2 + \Delta_j^2, \tag{10}$$

where $L_j$ is the radiance measured in band $j$; $SNR_j$ is the signal-to-noise ratio ($y/\sigma_y$); and $\Delta_j$ is the uncertainty of the calibration of band $j$.

We treat the uncertainties due to unknown forward model parameters as independent error sources by adding their contributions to $\mathbf{S}_y$, which is equivalent to standard error propagation:

$$\mathbf{S}_e = \mathbf{S}_y + \mathbf{K}_b \mathbf{S}_b \mathbf{K}_b^T, \tag{11}$$

where $\mathbf{K}_b$ is the Jacobian of the model unknowns, which expresses the change in modeled TOA radiance in the $j$-th instrument channel for a small change in the $k$-th unknown model parameter. It is expressed by:

$$\mathbf{K}_{j,k}^b = \{\frac{\delta y_j}{\delta b_k}\}. \tag{12}$$

$\mathbf{S}_b$ comprises uncertainties due to unknown, not retrieved parameters of the forward model. Following Thompson et al. (2018), they can be attributed to the surface, the instrument and the atmosphere. Their classification accounts for sky view effects, intrinsic error in absorption line intensities of water vapor, systematic calibration and radiative transfer uncertainty, and non-systematic radiometric uncertainty. We adopt their values for sky view effects and the water vapor absorption intensity and cover errors in liquid and solid water absorption line intensity by incorporating uncertainties of the imaginary part of the complex index of refraction $k$ presented by Kou et al. (1993). Since our sensitivity analysis is based on simulated data, we resign systematic and non-systematic errors. Table 2 gives an overview of the different error sources and their associated uncertainty values.

Table 2: Uncertainties due to unknown, not retrieved forward model parameters.

| Source | Elements | Value |
|---|---|---|
| Sky view factor | 1 | 10 % |
| Water vapor absorption intensity | 1 | 1 % |
| Liquid water absorption intensity | 1 | 2 % |
| Solid water absorption intensity | 1 | 2 % |

### 2.2.2. *A priori knowledge and first guess*

We assume no mentionable correlation between the different water phases so that a priori knowledge about their uncertainties is not taken into account. Hence, the diagonal entries of the a priori covariance matrix $S_a$ are set to relatively high values. This leads to an infinitesimally small weight of the first part of Eq. 5, and consequentially, the cost function only evaluates the measurement uncertainty and errors in the forward model parameters.

The inversion method generally requires a first guess solution for the state vector parameters. We use the a priori state vector $\mathbf{x_a}$ as first guess and start each iteration with the result from a band ratio retrieval for CWV (after Guanter et al. (2008a)). For the a priori state of liquid water, we calculate the normalized difference water index (NDWI) (Gao, 1996) and use its relationship to the liquid water path length presented by Gao (1996) to come up with a scaled value. A similar approach is taken into account for the a priori value of the ice path length. Here, we calculate the normalized difference snow index (NDSI) (Hall et al., 1995) and apply the thresholds proposed by the MODIS snow products user guide to start the iteration either with 0.1 or 0 (Riggs and Hall, 2015). Additionally, the offset $a$ and slope $b$ from Eq. 3 have to be optimized and are initialized by approximating the surface reflectance. For this purpose, we use the TOA reflectance $\rho_{TOA}$ at both absorption feature shoulders ($\lambda_1$ and $\lambda_2$):

$$\rho_{TOA,\lambda} = \frac{\pi * L_{TOA,\lambda}}{S_{0,\lambda} * \mu_{sun}}, \tag{13}$$

where $S_{0,\lambda}$ is the wavelength dependent exoatmospheric solar irradiance. Now, $a$ and $b$ can be estimated by:

$$a = \rho_{TOA,\lambda_2} - \frac{(\rho_{TOA,\lambda_1} - \rho_{TOA,\lambda_2}) * \lambda_2}{\lambda_1 - \lambda_2}, \tag{14}$$

$$b = \frac{(\rho_{TOA,\lambda_1} - \rho_{TOA,\lambda_2})}{\lambda_1 - \lambda_2}. \tag{15}$$

*2.2.3. Retrieval uncertainty*

The retrieval error covariance matrix $\mathbf{S}_x$ is obtained during the iteration procedure and provides information about the retrieval uncertainty and the error correlation between the retrieved state vector parameters. According to Rodgers (2000), the square root of the diagonal entries of $\mathbf{S}_x$ gives the retrieval error in the unit of the respective state vector parameter. It is equivalent to the standard deviation of the retrieved quantity. To enable an interpretation of the error correlation, we apply a normalization or rescaling leading to an error correlation matrix $\sum(i, j)$ (Govaerts et al., 2010):

$$\sum(i, j) = \frac{\mathbf{S}_x(i, j)}{\sqrt{\mathbf{S}_x(i, i) * \mathbf{S}_x(j, j)}}. \quad (16)$$

The equation for $\sum(i, j)$ results from the definition of the error covariance. If $\sum(i, j) \rightarrow +1$, the uncertainties of the state vector parameters are correlated, meaning an overestimation or underestimation of $i$ leads to the same for $j$. If $\sum(i, j) \rightarrow -1$, the uncertainties are anticorrelated, that is, an overestimation or underestimation of $i$ leads to the opposite for $j$. If $\sum(i, j) \rightarrow 0$, an error in the retrieval of $i$ does not effect the retrieval of $j$. The reliability of this approach including some examples can be found in Wagner et al. (2010).

## 3. Materials

We use both simulated and measured data from imaging spectrometers for evaluating the performance of the retrieval algorithm. First, we conduct a sensitivity analysis on simulated EnMAP data since the instrument is not launched yet. The workflow of the simulation is described in the following Section 3.1. Subsequent, Section 3.2 shortly presents the characteristics and chosen datasets of both the airborne AVIRIS-C and the spaceborne CHRIS-PROBA sensors, which we additionally use to validate the retrieval.

### *3.1. Simulation of EnMAP spectra*

For the sensitivity analysis, we used a unique coupling of the leaf reflectance model PROSPECT (Jacquemoud and Baret, 1990), the 3D canopy reflectance model Hyperspectral Simulation of Canopy Reflectance system (HySimCaR) (Kuester et al., 2014) and the sensor model EnMAP end-to-end Simulation tool (EeteS) (Segl et al., 2012) to simulate EnMAP-like TOA radiance spectra of 3D cereal canopies with known CWV and leaf water content (LWC) (Figure 2). The main focus is to assess the retrieval of CWC from vegetated agricultural surfaces. Therefore, we scaled up LWC to canopy level by multiplying with the leaf area index (LAI) (Clevers et al., 2010), which was calculated during the HySimCaR simulations.

EnMAP is a push-broom imaging spectrometer, which is scheduled for launch in 2021 and scientifically led by the GFZ German Research Centre for Geosciences (Guanter et al., 2015). It is a high performance scientific mission leading to Level 2A products including an open data policy. EnMAP will be in sun-synchronous orbit carrying two cameras: a VIS/NIR camera covering 420-1000 nm with a mean SSI of 6.5 nm and a SWIR camera covering 900-2450 nm with a mean SSI of 10 nm. The instrument has a swath width of 30 km and a spatial sampling distance (SSD) of 30 m. The mission lifetime is scheduled for 5 years.

Table 3: Parameter values used for PROSPECT simulations with all possible permutations resulting in 360 simulated reflectance signatures.

| $\mathbf{C}_{ab}$ [$\mu$g/cm$^2$] | $\mathbf{C}_{ar}$ [$\mu$g/cm$^2$] | $\mathbf{C}_{brown}$ [0-1] | $\mathbf{C}_w$ [cm] | $\mathbf{C}_m$ [m$^2$/$^2$] | **N** [0-1] |
|---|---|---|---|---|---|
| 20 | 5 | 0.0 | 0.006 | 0.002 | 1.0 |
| 30 | 15 | 0.5 | 0.012 | 0.008 | |
| 40 | 25 | 1.0 | 0.018 | | |
| 50 | | | 0.024 | | |
| | | | 0.030 | | |

*3.1.1. Modeling at leaf level - PROSPECT simulations*

PROSPECT is a leaf RTM, which simulates reflectance as a function of leaf bio-physical and -chemical parameters (Jacquemoud and Baret, 1990). It is coupled to canopy RTM's such as SAIL, like in PROSAIL, which also includes canopy structural elements (Jacquemoud et al., 2009), or SCOPE, which is a variation of PROSAIL including photosynthesis (van der Tol et al., 2009). Here, we used PROSPECT to generate leaf reflectance and transmittance spectral signatures with varying leaf water content ($C_w$), chlorophyll content ($C_{ab}$), carotenoid content ($C_{ar}$), brown pigments ($C_{brown}$), dry matter content ($C_m$) and leaf mesophyll structure (N) (Table 3). The parameter values were varied according to experiences from several years of in-situ measurements and literature values like from Jacquemoud and Baret (1992) or Xiao et al. (2014).

*3.1.2. Modeling at canopy level - HySimCaR simulations*

HySimCaR has been developed in the context of the EnMAP mission. This spectral, spatial and temporal simulation system consists of detailed virtual 3D cereal canopies for different phenological stages, whose geometries are linked to corresponding spectral information. The system enables the simulation of realistic bidirectional reflectance spectra on the basis of virtual 3D scenarios by incorporating any possible viewing position with ray tracing techniques. The sampling of the virtual 3D canopies is performed by the aDvanced Radiometric rAy Tracer (DRAT), an efficient MCRT (Monte Carlo Ray Tracing) software that was developed by Lewis (1999). DRAT calculates the canopy reflectance based on 3D descriptions with linked spectral properties, predefined camera imaging properties and illumination conditions using reverse ray tracing. The reflectance results conform to case 1 (bidirectional) of Nicodemus et al. (1977) using a planar camera model with orthographic methods and a directional illumination source. Since the third phase of RAMI (RAdiation transfer Model Intercomparison, RAMI-3 (Widlowski et al., 2007)) the DRAT model belongs to a series of credible 3D MCRT models. HySimCaR has been validated with respect to structural and spectral accuracy using three cereal types, including wheat *(Triticum aestivum)*, rye *(Secale cereale)* and barley *(Hordeum vulgare)*, and 13 different phenological stages between leaf development and senescence (after

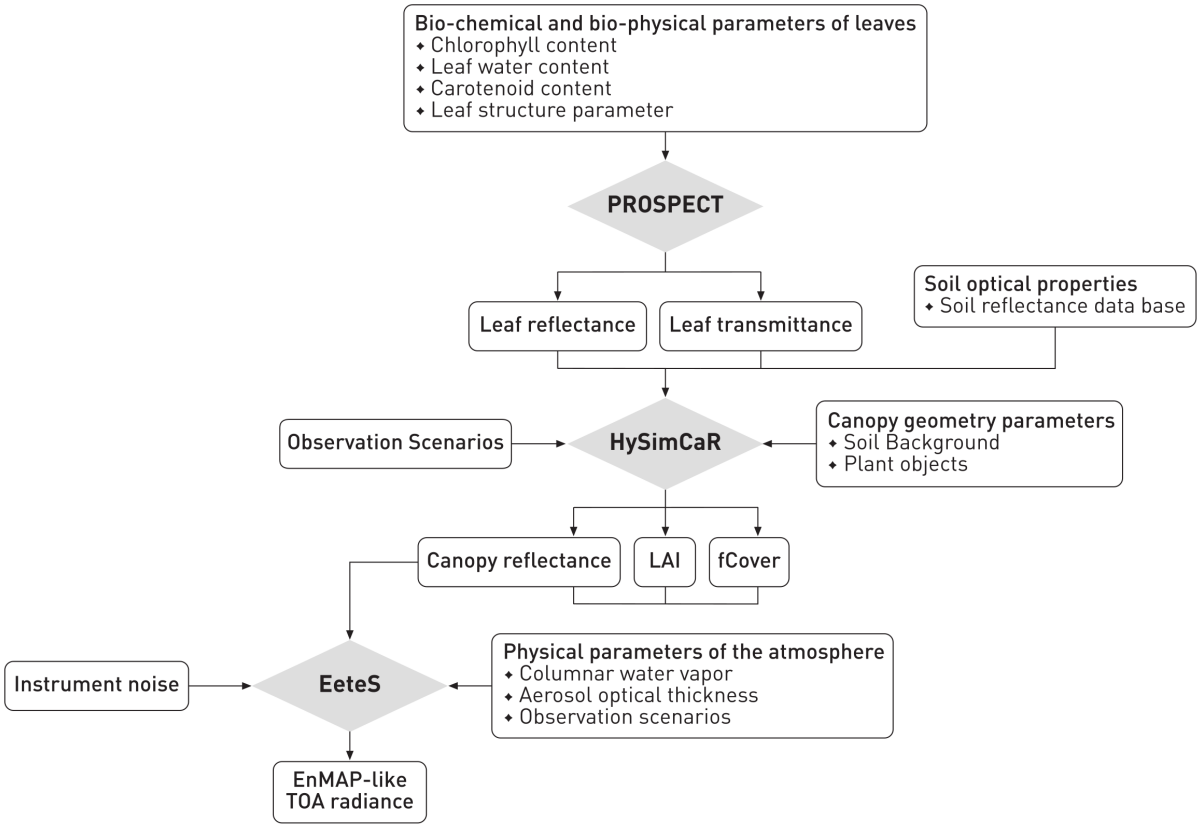


Figure 2: Structure chart of the simulation process to gain EnMAP-like vegetation canopy TOA radiance data.

the phenological scale system of Meier (1997)). A detailed description of HySimCaR, including the entire virtual plant and canopy build up, the virtual sampling process and its validation can be found in Kuester (2011); Kuester et al. (2014), and Spengler (2014). In addition, the model has already been used for several applications found in Kuester et al. (2017); Kuester and Spengler (2018), and Spengler et al. (2011, 2013). Based on the model, the influence of plant and canopy architecture on cereal canopy reflectance, the anisotropic behaviour of cereal canopy reflectance and its inter-annual variations were investigated by Kuester and Spengler (2018). Additionally, the influence of vegetation cover on the prediction of soil spectral features was investigated and quantified by Kuester et al. (2017).

We modeled 72 structurally different virtual canopies varying in canopy phenology and architecture (see Table 4 for respective HySimCaR parameter values). The values of the virtual canopies were chosen to balance between natural variety, management and computational costs. Phenology, the number of plants per meter of seeding row, the number of tillers per plant and the distance between the rows are parameters determining canopy density and volume that influences the shape of the reflectance signal mainly due to leaf pigment absorption and volume scattering. The relative orientation of the seeding rows against the sun azimuth angle (SAA) influences the brightness of the whole reflectance signal due to different sunlit and shading effects. The spectral properties of the soil background were kept constant, as the focus of this study is on the vegetation parameters. As a consequence, the retrieval of liquid water content from vegetated surfaces is less violated and is assumed to report only the amounts included in the canopy. This enables a higher retrieval accuracy and a direct interpretation of the results with respect to plant conditions. Otherwise, the algorithm would likely report additional liquid water amounts in terms of soil moisture or water included in minerals. Also, overlapping absorption features of minerals could impact the liquid water retrieval. Only the 3D structure of the soil background was included to consider the typical sunlit and shading effects. LAI and fCover were calculated directly from the 3D geometry of the virtual canopies and range between 0.32 and 3.17 for LAI and between 0.18 and 0.87 for fCover. The values of both parameters are almost equally distributed. All virtual canopies were coupled with PROSPECT leaf reflectance and transmittance. This sums up to 25,920 different leaf-canopy combinations that were sampled virtually. All resulting canopy reflectance spectra contain 467 continuous spectral bands (4 nm SSI) between 400 nm and 2448 nm with the exception of the

Table 4: Parameter values used for HySimCaR simulations resulting in 72 virtual cereal canopy scenarios. (Meier, 1997)

| Row orientation against SAA | Plants per meter row | Tillers per plant | Row distance | Phenology (Meier, 1997) |
|---|---|---|---|---|
| 0° | 13 | 5 - 3 dev. | 13 cm - 17 cm | 24-25 late tillering |
| 30° | 15 | | 22 cm - 26 cm | 37-39 stem elongation |
| 60° | 17 | | | 41-43 late stem elongation |
| 90° | | | | |

ranges of atmospheric absorption ([1352 nm, 1416 nm] and [1824 nm, 1936 nm]).

*3.1.3. Modeling at sensor acquisition level - EeteS simulations*

Based on HySimCaR model outputs, EnMAP TOA radiance spectra were simulated using EeteS (Segl et al., 2012). This tool simulates the entire image data acquisition, calibration and processing chain from spatially and spectrally oversampled data to intermediate Level-1A (systematically-corrected) raw data and to the final EnMAP products, such as Level-1B (radiometrically-corrected, spectrally- and geometrically-characterized radiance), Level-1C (orthorectified Level-1B product) and Level-2A data. Data acquisition consists of a sequential processing chain represented by four independent modules: atmospheric, spatial, spectral, and radiometric. These modules allow flexible customization of a wide range of simulation input parameters. They are coupled with a backward simulation branch consisting of calibration modules, such as nonlinearity, dark current, and absolute radiometric calibration, and a series of preprocessing modules such as radiometric calibration, co-registration, orthorectification, and atmospheric correction. Since the modeled data base only consists of a collection of reflectance spectra, the simulation of the two spaceborne sensors is only performed in terms of spectral and radiometric characteristics. No spatial simulation was performed with EeteS assuming that the pixel size already is 30 m. The atmospheric simulation was performed with settings for the end of May using identical parameters for all 25,920 canopy reflectance spectra with respect to viewing geometry and physical parameters (AOT: 0.2, rural aerosol model, HSF: 0 km). Only CWV was varied between 1.9 and 2.2 $\frac{g}{cm^2}$. To calculate the measurement error covariance matrix $S_e$ within the retrieval algorithm, we obtained the EnMAP SNR from Guanter et al. (2015). EeteS provides the option to add instrument noise to the simulated TOA radiance (Figure 2). But since we assume no significant influences of noise effects on the three phases retrieval, we abstained from including them (see Section 4.1.3).

*3.2. Imaging spectroscopy measurements*

To extend the analysis on real data, we chose two additional datasets of imaging spectroscopy measurements for assessing the retrieval results. The first one is an airborne AVIRIS-C image acquired over a mountainous area in the Sierra Nevada, California, on 02/24/2015. The particular aim is to show the possibility of the algorithm to map snow/ice extent. We generated two subsets of the acquisition: one containing vegetated agricultural areas and rock surfaces in equal parts covering 35.70°N - 35.76°N and 118.07°W - 118.13°W, and another consisting of partly snow- and forest-covered mountain ranges reaching from 35.57°N to 35.65°N and from 118.04°W to 118.13°W. The first subset shows a surface elevation of 400 m to 600 m for the vegetated areas and up to 1700 m for the mountainous parts. The second, more elevated region reaches up to 2300 m HSF for the highest snow-covered mountains.

AVIRIS-C has a similar wavelength range and SSI to the EnMAP sensor but varying ground sampling distance due to different flying altitudes (Green et al., 1998). It is installed on the NASA ER-2 research aircraft so that AVIRIS-C is able to acquire data from a height of up to 20 km, which results in an SSD of 20 m. The coefficients to calculate the measurement uncertainty were taken from the Python ISOFIT repository and the AVIRIS-C SNR needed for the retrieval algorithm was calculated according to Thompson et al. (2018).

To demonstrate the applicability to satellite images we also used a spaceborne CHRIS-PROBA dataset from the ESA SPARC'03 campaign in Barrax, Spain, acquired on 07/14/2003. The image covers a mixture of agricultural areas and open soil so that it is well suited for the CWC retrieval analysis. The acquisition reaches from 38.97°N to 39.13°N and from 2.00°W to 2.19°W. There are no remarkable differences in surface elevation throughout the image as the Barrax region is part of a high plateau in south-east Spain.

CHRIS-PROBA is a push-broom imaging spectrometer featuring a swath width of 13.5 km and an SSD of 36 m in the hyperspectral mode. It has a spectral range covering 410 nm to 1050 nm and an SSI of 1.25 nm (at 400 nm) and 11 nm (at 1050 nm) (Barducci et al., 2005). Barducci et al. (2005) also provided the SNR required for the retrieval algorithm. Since CHRIS-PROBA is missing channels beyond 1050 nm, we used the 940 nm water absorption feature for the retrieval.

## 4. Results and discussion

*4.1. Retrieval from simulated EnMAP data - sensitivity analysis*

*4.1.1. Water vapor*

We first compare the results from the maximum likelihood estimation with the simulation input described in Section 3.1. We achieve a very good matching with the input values showing an $R^2$ of 0.99 and an RMSE of 0.007 $gcm^{-2}$ with an overall very slight underestimation of the CWV values (Figure 3a). Figure 3b illustrates the absolute CWV retrieval error as a function of simulated CWC from the three phases retrieval. For low CWC values of up to 0.02 $gcm^{-2}$, we find a negative error of around -0.01 $gcm^{-2}$ for the CWV retrieval. As it will be presented in Section 4.1.2, the retrieval clearly overestimates the CWC, especially for low vegetation canopy heights and small LAI. This causes the very slight underestimation of CWV for low CWC since the algorithm seems to attribute a very small fraction of CWV to nonpresent CWC. However, Figure 3b shows a clear linear trend of the CWV retrieval error from underestimation for low CWC values to an overestimation for higher CWC. This accords with the experience from band ratio CWV retrievals, which tend to even more overestimate CWV under the presence of high liquid water absorption (Thompson et al., 2015). To confirm this assumption, we additionally show the results from the a priori band ratio CWV retrieval (Figure 3c and Figure 3d). The values clearly more scatter around the 1:1-line with a tendency to overestimation and the absolute CWV retrieval errors are immensely higher. The retrieval is slightly biased due to the a priori state which is based on the overestimated CWV values. As a consequence, a very small overestimation of CWV for higher simulated CWC

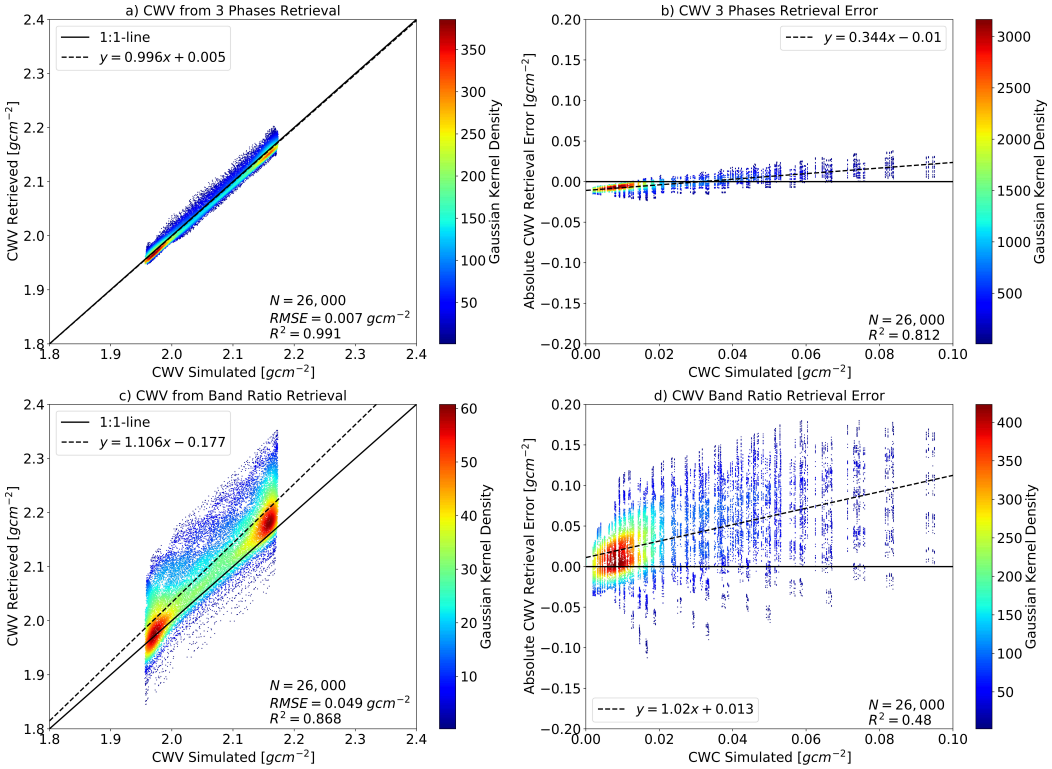


Figure 3: Comparison of derived CWV with the input of the HySimCaR + EeteS simulations. a) Results from the three phases retrieval. b) Absolute CWV retrieval error as a function of simulated CWC values for the three phases retrieval. c) Results from the band ratio retrieval. d) Absolute CWV retrieval error as a function of simulated CWC values for the band ratio retrieval.

still occurs (Figure 3b). However, our results accord with the outcomes of previous studies that estimating CWV and liquid water amounts in a simultaneous way improves the accuracy of atmospheric correction procedures since biases due to background reflectance are reduced (Gao and Goetz, 1995; Green et al., 1991; Thompson et al., 2015).

### *4.1.2. Canopy water content*

In the same way as for CWV, we compare retrieved CWC with the simulation input. Again, a very good correlation between retrieved and simulated values can be observed depicting an $R^2$ of 0.96 (Figure 4a). Though, the result shows a constant mean overestimation with a slope of approximately 3.37 and virtually no offset. This induces the relatively high RMSE of 0.07 $gcm^{-2}$. Nearly the same behavior was found by Wocher et al. (2018), whose CWC retrieval from TOC spectra is likewise based on the Beer-Lambert law too, but with a constant overestimation of around 3.52. They calibrated their retrieval model with simulated PROSPECT spectra and tested the approach on ASD measured in situ data and HyMAP images. This overestimation is due to volume scattering processes within the vegetation canopies, which the Beer-Lambert law cannot take into account (Zhang et al., 2011). Although Wocher et al. (2018) received accurate results, it has to be mentioned that both, their study and our simulations of EnMAP data, are based on spectra of more or less uniform canopies of low-lying cereal crops between tillering and late stem elongation and therefore, higher uncertainties might be assumed by applying such model calibration factors to more complex canopies and/or different observing conditions. Especially different observation geometries, such as those planned for EnMAP (off-nadir observations up to ±30° (Guanter et al., 2015)) lead to an increase of the uncertainties. Asner and Martin (2008) showed that LAI and viewing geometry most negatively impact the accuracy of the spectroscopic retrieval of especially CWC. The difficulty to transfer between different observation geometries largely stems from changing fractions of sunlit or shaded vegetation (opaque or translucent) or soil. Depending on the viewing angle, the sensor observes a different composition of the reflecting surfaces due to the path of radiation through the vegetation canopy. For this, more investigations would have to be made in order to be able to evaluate the transferability of the method to different observation geometries. Kuester and Spengler (2018) have analyzed the spectral influences of different canopy architecture and observation geometries on cereal canopy reflectance and found that the larger the fraction of the radiation reflected by the vegetation canopy, the stronger is the influence of the canopy architecture on the reflectance signal. A finding that can very likely also be assumed for other vegetation canopies such as pastures or shrublands. A detailed discussion of the influence of crop canopy architecture on the CWC three phases retrieval of arable lands and a test investigating possible modifications of the Beer-Lambert law are provided in Section 4.4.

However, Figure 4b gives an impression of the advantages of imaging spectroscopy with respect to multispectral instruments. The correlation between retrieved CWC and NDWI is

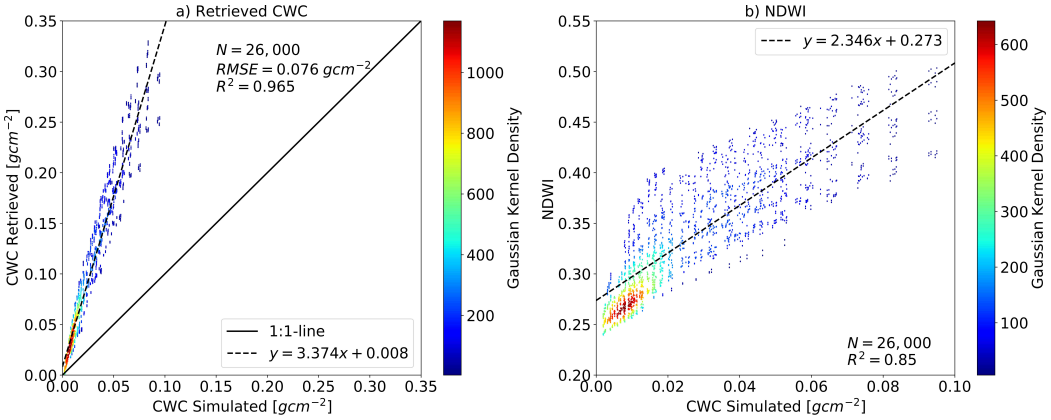


Figure 4: Comparison of derived CWC from the three phases retrieval with a) the input of the HySimCaR + EeteS simulations and b) the previously calculated NDWI, which has been used to build the a priori state of liquid water.

clearly lower with an $R^2$ of 0.85 showing a stronger scattering around the regression line. Consequentially, we assume that the three phases approach can better capture changes in CWC than multispectral indices are able to and thus, offers a high potential for accurate vegetation analysis.

#### *4.1.3. Surface reflectance*

We additionally used the CWV and CWC retrieval results to calculate atmospherically corrected surface reflectance spectra. This enables a quantitative comparison with the input canopy reflectance spectra simulated by HySimCaR. We evaluate the wavelength range around the used water absorption feature at 1140 nm (Figure 5). Very good results can be observed for both the modeled TOA radiance and the surface reflectance. The residual errors range within 0.5 % for low CWC and within 1 % for high CWC, which makes the results similar to those obtained by Thompson et al. (2015).

We achieved the results based on noise free simulated TOA radiance spectra. Adding instrument noise to the simulations leads only to a marginal decrease of retrieval accuracy. Figure 6 shows the norm of the mean residual errors of all simulated spectra for both the modeled TOA radiance and the retrieved surface reflectance. Again, we evaluate the absorption feature around 1140 nm separated in results for spectra containing either low or high CWC. The dashed lines represent simulations with additional instrument noise while the solid lines illustrate the simulations without noise used for our sensitivity analysis. Both modeled TOA radiance and retrieved surface reflectance show a similar behavior when noise is added to the simulations. For low CWC the residual errors increase by a factor of 2 to 4, whereas for high CWC the errors are only marginally higher. Especially the surface reflectance retrieval seems to be nearly unaffected by instrument noise under the presence of high CWC. Furthermore, the retrieval accuracy of CWV and CWC only slightly decreases when noise is added to the simulations (Table 5). The $R^2$ still shows values of 0.98 for CWV and 0.93 for CWC, respectively, indicating a very good correlation. Although the RMSE for CWV rises of about 23 %, the absolute retrieval error still is below 0.5 % of the mean retrieved CWV. The RMSE for CWC even rises about only 2 % under the influence of instrument noise. These results justify our previous assumption not to add instrument noise to the simulations.

Table 5: Regression coefficients and correlation metrics for retrieved CWV and CWC for simulations including instrument noise and for noise free simulations used for the sensitivity analysis.

| | Slope | Offset | $R^2$ | RMSE |
|---|---|---|---|---|
| CWV | 0.9969 | 0.0053 | 0.9919 | 0.0077 |
| CWV (noise) | 0.9828 | 0.0348 | 0.9869 | 0.0095 |
| CWC | 3.3746 | 0.0082 | 0.9650 | 0.0767 |
| CWC (noise) | 3.4583 | 0.0044 | 0.9328 | 0.0784 |

#### *4.1.4. Correlation errors*

Based on Eq. 16 we calculated the correlation error matrix for the synthetic EnMAP dataset. Figure 7 shows the correlation of the retrieval errors between the state vector parameters, which are all optimized during the iteration procedure. Errors in the estimation of slope and offset of the linear reflectance continuum clearly influence the CWC retrieval featuring coefficients of 0.93 and -0.92, respectively. Otherwise, the CWV retrieval seems to be nearly uncorrelated with the CWC derivation. This justifies the use of the maximum likelihood approach instead of the optimal estimation method at least for the CWV and CWC retrieval. However, the correlation coefficients for offset and slope indicate that a priori information about both quantities is needed to increase the accuracy of the retrieval. In general, if a priori uncertainties are known and free of biases, adding a priori knowledge, that is, applying optimal estimation, can significantly improve the retrieval results (Rodgers, 2000).

### *4.2. Retrieval from AVIRIS-C data*

Figure 8b-c shows the retrieved CWV and CWC maps for the AVIRIS-C Sierra Nevada vegetation subset. As previously shown in Green et al. (2006), the distribution of the CWV values obviously matches the texture of the surface elevation in an anticorrelated way and CWC is clearly higher for vegetated areas compared with rock surfaces (also see Thompson et al. (2015)). The derived CWV ranges from 0.78 gcm$^{-2}$ and less

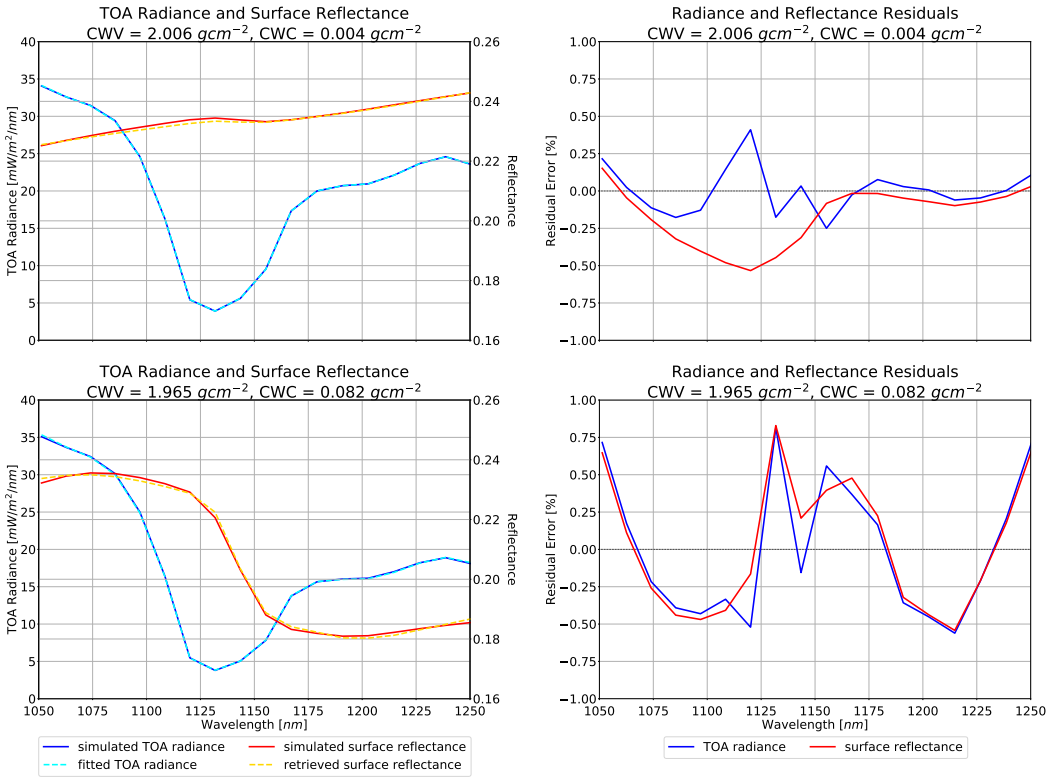


Figure 5: Results for the TOA radiance spectral fit and the surface reflectance retrieval from simulated EnMAP data for the water absorption feature at 1140 nm. Left panel: simulated and fitted TOA radiance as well as simulated and retrieved surface reflectance. Right panel: relative residual errors for both quantities. Upper panel: low CWC amount. Lower panel: high CWC amount.

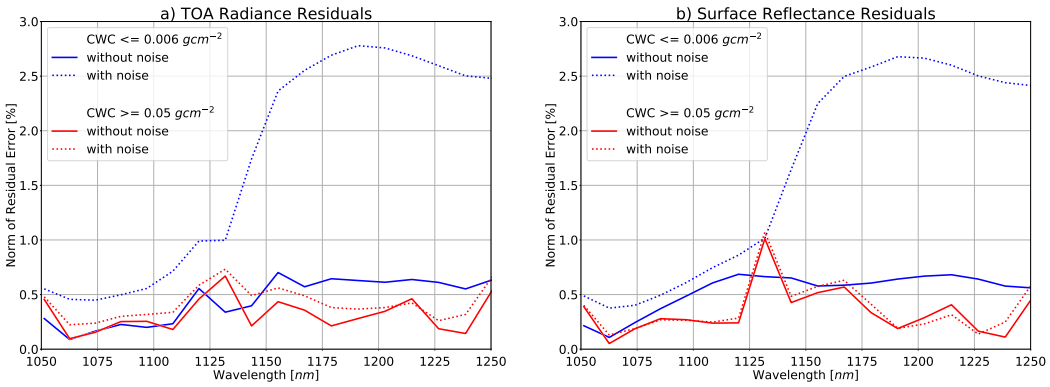


Figure 6: Norm of the mean residual errors of all simulated spectra for a) the modeled TOA radiance and b) the retrieved surface reflectance. Blue lines represent low CWC <= $0.006 gcm^{-2}$, red lines illustrate high CWC >= $0.05 gcm^{-2}$. Dashed lines represent simulations with additional instrument noise, solid lines illustrate simulations without noise used for the sensitivity analysis.

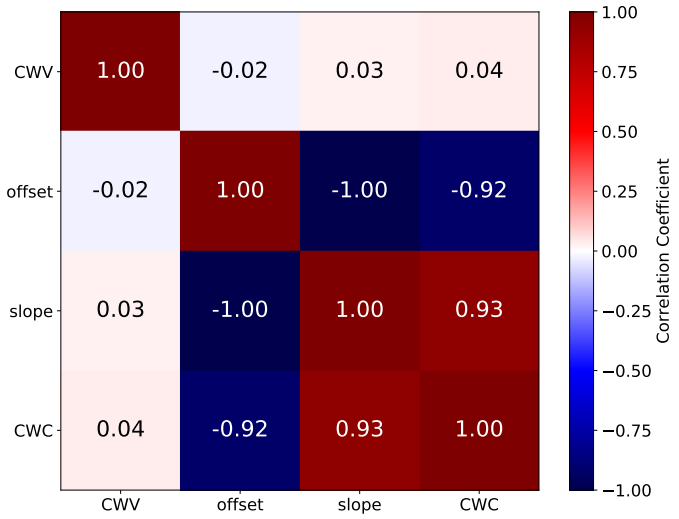


Figure 7: State vector correlation error matrix for the three phases retrieval from the simulated EnMAP data.

for the highest elevations of up to 1700 m and 0.90 gcm$^{-2}$ and more for lower elevated areas of around 500 m. This is plausible when comparing with AERONET data. The nearest station at a distance of approx. 250 km in Fresno, CA (36.8°N, 119.8°W, 100 m surface elevation) shows a mean CWV of 0.91 gcm$^{-2}$ and a maximum value of 0.98 gcm$^{-2}$ for February 24, 2015 (AERONET, 2019). The retrieved CWC of 0-0.2 gcm$^{-2}$ is also meaningful when comparing to the results from the sensitivity analysis (Section 4.1.2).

We additionally produced uncertainty maps from the a posteriori covariance matrix showing the retrieval errors for CWV and CWC (Figure 8d-e). Overall, CWV shows lower errors than CWC due to less variance within the retrieved values, which was also shown by the sensitivity analysis on simulated data. Furthermore, the type of surface has not that much influence on the amount of vapor in the atmosphere. This influence can be seen in the CWC uncertainty map yielding the highest retrieval errors over dark surfaces, e.g., the shady sides of the mountains, since the CWC estimation depends on the signal strength of the surface reflection. Also, a general issue of RTMs is that they are not able to realistically simulate shaded areas.

For a continuative evaluation, we compared the retrieved CWC with the NDWI, which has been previously calculated to build the a priori state of liquid water (see Section 2.2.2) (Figure 9). We achieve an $R^2$ of 0.71, which indicates a good correlation between derived CWC and NDWI and confirms the plausibility of the three phases retrieval result.

Although the solid water phase was not considered for the sensitivity analysis, we included an appropriate dataset to apply the algorithm on snow-covered surfaces. Figure 10b-d shows the retrieved maps for the three water phases for the AVIRIS-C snow/ice subset. To improve the interpretation of spatial trends of the three phases, we produced a combined RGB map (Figure 10e). CWV, CWC and ice are displayed in red, green, and blue, respectively. Consequentially, turquoise colors depict melting snow since both ice and liquid water are present. Again, the CWV values anticorrelate with surface elevation and the value range of CWV (0.72-0.88 gcm$^{-2}$) likewise fits well to the AERONET observations at Fresno mentioned before (AERONET, 2019). The derived CWC of up to 0.4 gcm$^{-2}$ increases for surfaces covered by wet snow and accords with typical value ranges for liquid water observed by Green et al. (2006). The distribution of snow and ice-covered areas corresponds well with the false-color image and the results with many pixels showing around 0.5 gcm$^{-2}$ or enormously more are in a good compliance with typical values for dry and wet snow presented by Green et al. (2006).

We also compare the derived ice amounts with the NDSI, which results in a very good correlation with an $R^2$ of 0.94 (Figure 11). The fitted polynomial regression indicates that the three phases retrieval is able to better distinguish between medium and high ice amounts compared to the NDSI, which becomes saturated at a value of around 0.9.

### *4.3. Retrieval from CHRIS-PROBA data*

Figure 12b-d shows the retrieval results for the CHRIS-PROBA Barrax dataset incorporating the CWV and CWC maps from the three phases retrieval. The true-color image is supplemented by the indicators of ground-truth data conducted during the ESA SPARC'03 campaign, which amongst others contain CWC measurements. Additionally, we present a CWV map derived from the a priori band ratio retrieval (see Section 2.2.2). As likewise shown in Thompson et al. (2015), the CWV map from the three phases retrieval is much smoother and physically-plausible. In contrast, the CWV map from the band ratio approach has clear biases in form of textures according with vegetated areas indicating a higher sensitivity to background reflectance. Also low-frequency striping patterns are visible, which have been previously observed by Guanter et al. (2008b). The result from the algorithm presented in our study is nearly free of these influences. Cloud pixels have been excluded from the retrieval and areas of cloud shadow have to be treated carefully within the analysis since retrieved CWV generally shows a strong positive bias for these pixels (Barducci et al., 2004).

As one major result, the three phases retrieval leads to a decoupling of retrieved CWV from apparent CWC. Already recognizable in the maps of Figure 12, the influence of present surface liquid water on the CWV retrieval declines compared with the band ratio retrieval. This is underlined by both the decreasing slope and $R^2$ from 0.49 to 0.08 and from 0.38 to 0.08, respectively, when comparing retrieved CWV with retrieved CWC for the different methods (Figure 13). This trend was also observed by Thompson et al. (2015).

The derived CWC map provides a clear distinction of agricultural areas and bare soil as pixels with high water content can be distinguished well from the surroundings. Furthermore, the validation with the CWC field measurements yields a good correlation resulting in an $R^2$ of 0.8 (Figure 14). The overestimation of CWC by the Beer-Lambert model is clearly visible and varies depending on the crop type, which results in a remarkable forming of clusters. For example, the measured CWC of garlic and alfalfa is in a similar range, but the retrieval overestimates

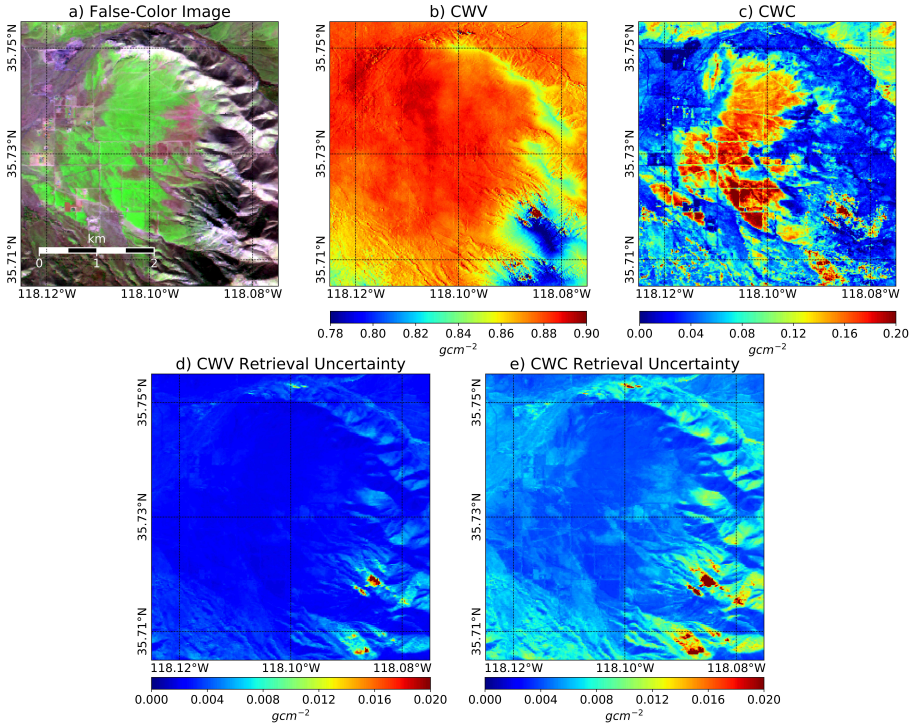


Figure 8: Results for the three phases retrieval from the AVIRIS-C Sierra Nevada vegetation subset, supplemented by the uncertainty maps from the a posteriori covariance matrix. a) False-color image (RGB: 1602/870/560 nm). b) CWV map. c) CWC map. d) CWV uncertainties. e) CWC uncertainties. The pixel values of the uncertainty maps represent the standard deviation in the unit of the retrieved parameter.

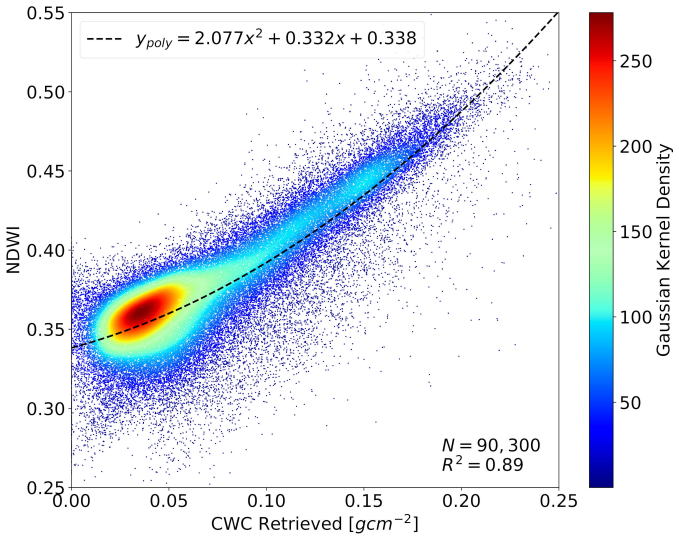


Figure 9: Comparison of NDWI with retrieved CWC from the AVIRIS-C Sierra Nevada vegetation subset.

most of the alfalfa CWC by a factor of 2 to 3. The clusters indicate the different crop type architectures and penetration depths and thus, the varying ability to detect CWC. Pasqualotto et al. (2018) recently developed two new hyperspectral indices to retrieve CWC: the water absorption area index (WAAI) and the depth water index (DWI). They also used the dataset of field measurements from the ESA SPARC'03 campaign in Barrax, Spain, acquired on 07/14/2003, but in combination with atmospherically corrected airborne HyMap data. They achieved an $R^2$ of 0.8 for the WAAI and 0.7 for the DWI. Hence, the result from the three phases retrieval ranges in the same order of magnitude and even outperforms one of the proposed hyperspectral indices.

Another substantial fact is that the algorithm is able to meaningfully map CWV and CWC without having the right shoulder of the 940 nm water absorption feature at its disposal since CHRIS-PROBA is missing channels beyond 1050 nm. However, these missing bands can lead to higher retrieval uncertainties when looking at the validation of absolute values. This is also expressed by the uncertainty maps from the a posteriori matrix, which show much higher uncertainties for both CWV and CWC than for the AVIRIS data. Especially, a strong correlation between retrieved CWC and retrieval error is observable (Figure 12e-f). Another error source within the CWV retrieval are the miscalibration trends of CHRIS-PROBA in the NIR wavelength range. This issue was reported by Guanter et al. (2005) who stated that the resulting underestimation of the signal cannot be used for common radiative transfer algo-

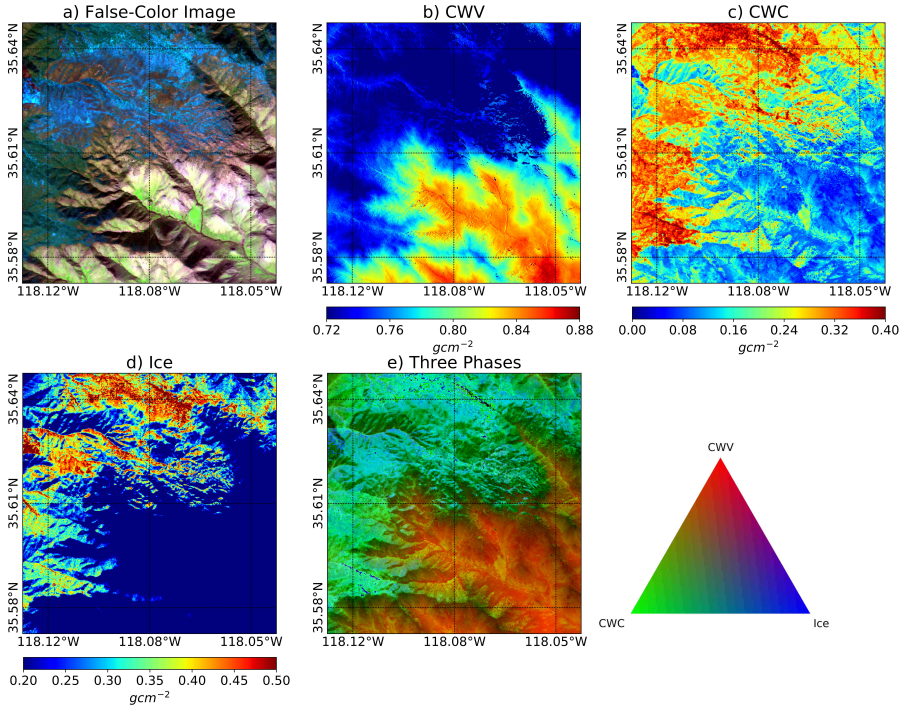


Figure 10: Results for the three phases retrieval from the AVIRIS-C Sierra Nevada snow/ice subset. a) False-color image (RGB: 1602/870/560 nm). b) CWV map. c) CWC map. d) Ice map. e) Combined three phases map (RGB: CWV/CWC/Ice).

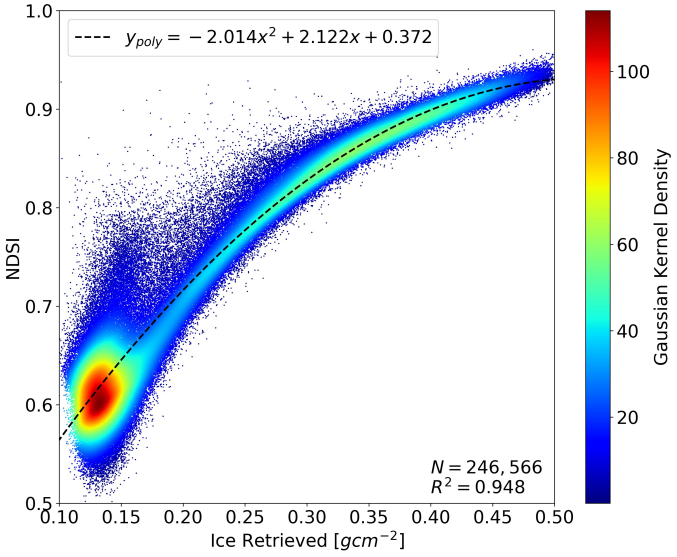


Figure 11: Comparison of NDSI with retrieved ice path lengths from the AVIRIS-C Sierra Nevada snow/ice subset.

rithms, which instead have to be supplemented by empirical line approaches to obtain useful results.

### *4.4. Interpretation of CWC retrieval results*

Wocher et al. (2018) used the regression slope for calibrating their CWC retrieval results, but our study indicates that this factor cannot be seen as a global calibration. As shown in Figure 14, the overestimation varies depending on the vegetation type and the according characteristics. We further investigate this with some analysis on the simulated EnMAP data. As a result, a critical factor influencing the overestimation is the vegetation canopy height (Figure 15a). Increasing the height of simulated cereal plants from 12 cm to 66.5 cm leads to a decrease in regression slope from 5.28 to 3.05. Furthermore, the overestimation decreases from 3.77 to 2.88 for increasing LAI from less than 2 to more than 3 (Figure 15b). On one hand, the overestimation can be attributed to volume scattering processes within the canopy, which the Beer-Lambert law is not able to account for (Zhang et al., 2011). These are very special effects in vegetation canopies due to the multitude of scattering objects, e.g., leaves, and their ability to transmit radiation (Kuester and Spengler, 2018). On the other hand, it can be stated that the higher the modeled canopies and the LAI are, the better is the accuracy of retrieved CWC. Roberts et al. (1998) showed that LAI and vegetation canopy liquid water amounts are well correlated. Consequentially, we assume that with increasing LAI the volume scattering effect indeed gets stronger, but since the liquid water contents simultaneously increase, the additional amounts retrieved by the Beer-Lambert law get smaller compared to the actual CWC and lead to a higher retrieval accuracy. This fits to

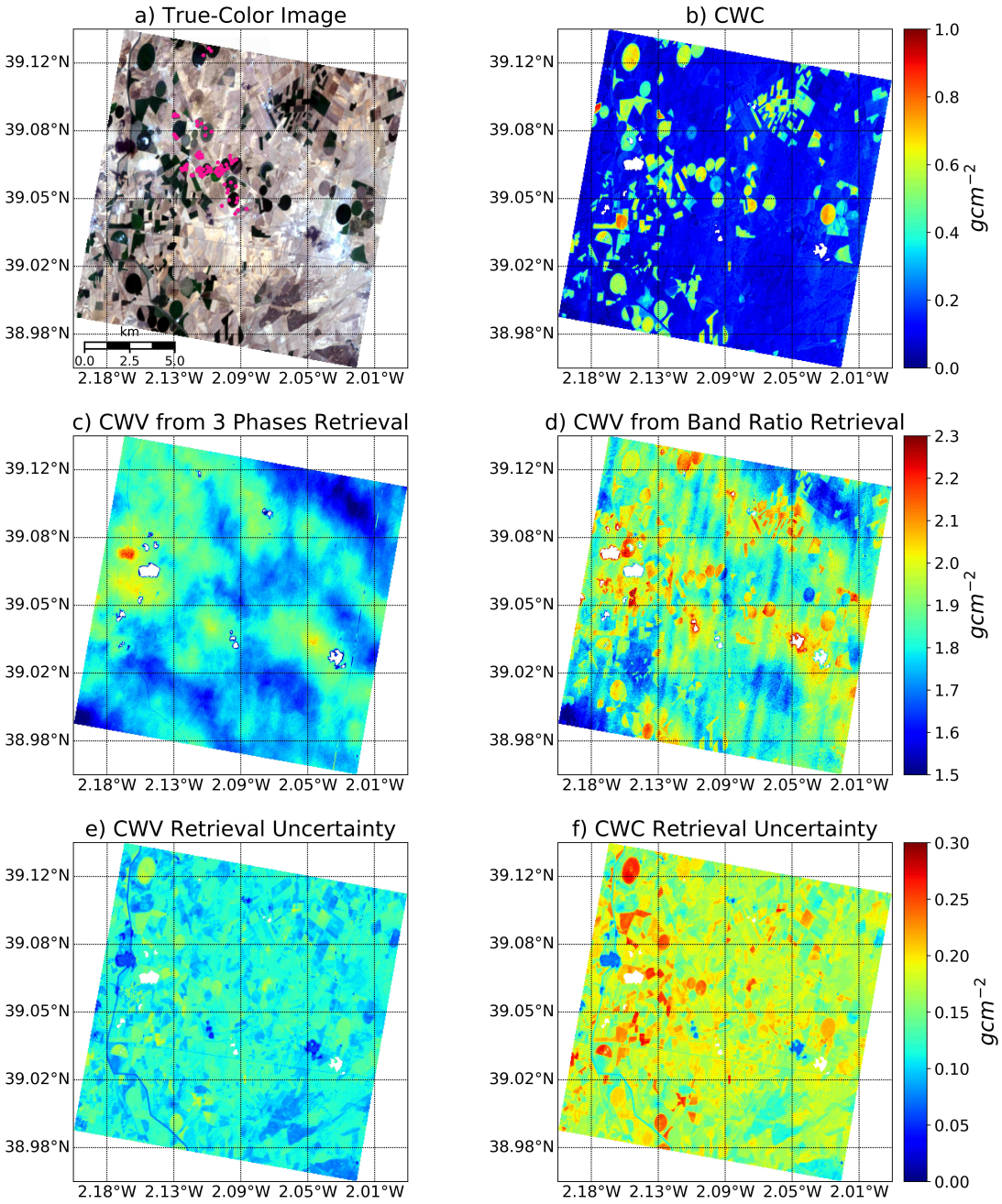


Figure 12: Retrieval results from the CHRIS-PROBA Barrax dataset, supplemented by the uncertainty maps from the a posteriori covariance matrix. a) True-color image with pink colored points representing locations of field measurements (RGB: 653/563/481 nm). b) CWC map derived from the three phases retrieval. c) CWV map derived from the three phases retrieval. d) CWV map derived from the a priori band ratio retrieval. e) CWV uncertainties. f) CWC uncertainties. White colored pixels indicate masked clouds, which have been excluded from the retrievals. Except for the upper panel, each colorbar accounts for both left and right panel. The pixel values of the uncertainty maps represent the standard deviation in the unit of the retrieved parameter.

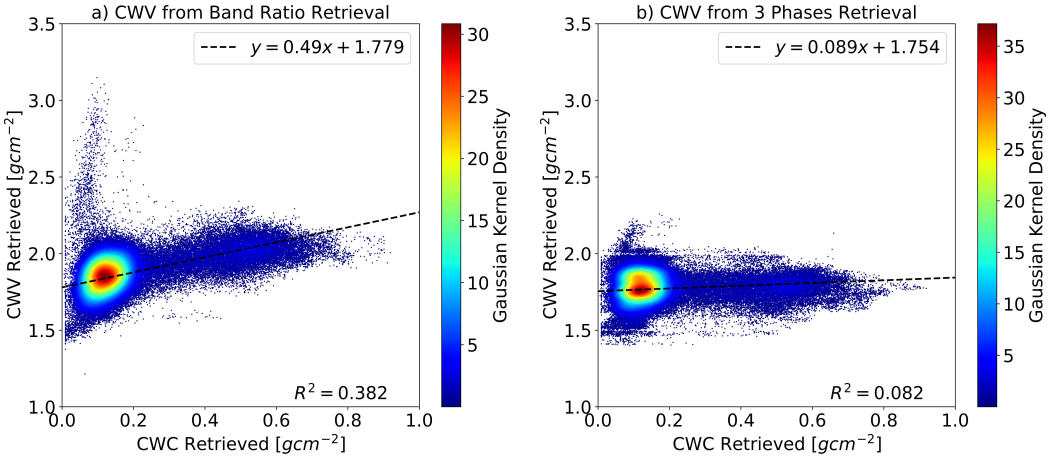


Figure 13: Comparison of retrieved CWV with retrieved CWC for different retrieval methods. a) Band ratio retrieval. b) Three phases retrieval.

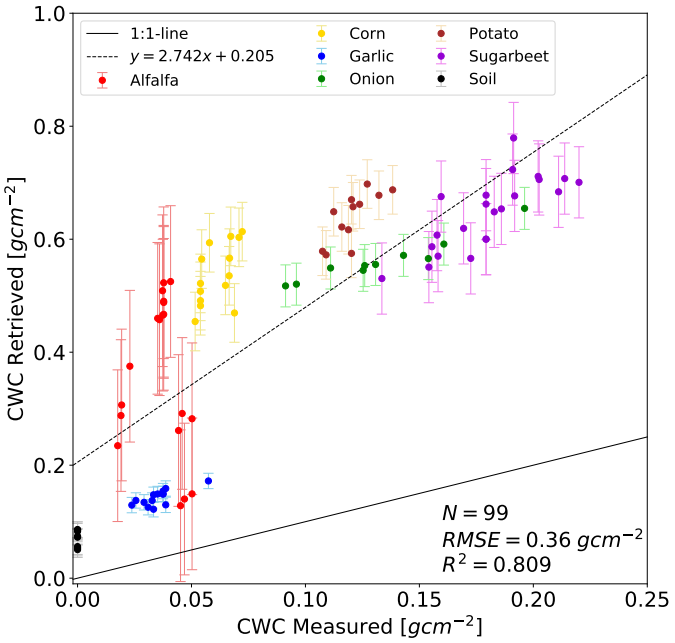


Figure 14: Comparison of retrieved CWC with measured CWC from the Barrax SPARC'03 field campaign. Error bars indicate the standard deviation of retrieved CWC.

the findings of Wocher et al. (2018) who got best results in the early young growth stages when most of the scattering objects in the canopy are leaves. In general, the more opaque stalks and ears are present in the canopy, the lower is the retrieval accuracy.

We added a test of NIR reflectance as an indicator of volume scattering by calculating the NIR reflectance of vegetation (NIRv) for each spectrum. This index was presented by Badgley et al. (2017) and is related to photon escape probability, i.e., NIR reflectance, and corrects for the non-green parts of the pixel:

$$NIRv = (NDVI - 0.08) * \rho_{TOA,\lambda_{NIR}}. \quad (17)$$

It is calculated as the product of normalized difference vegetation index (NDVI) and NIR TOA reflectance $\rho_{TOA,\lambda_{NIR}}$ at $\lambda_{NIR} \sim 780\ nm$. Badgley et al. (2017) proposed to substract 0.08 from the NDVI values to account for bare soil. Figure 16 shows the NIRv compared with LAI for different canopy heights. The NIR reflectance is well correlated with LAI yielding an $R^2$ of 0.81 and clearly increases for higher LAI. The canopy height seems to have less effect on the NIRv. Only for very small vegetation the NIR reflectance is substantially lower. Concluding, we assume that the volume scattering effects are mainly correlated with LAI and not necessarily with canopy height. Thus, a future approach will be to supplement the surface reflectance model based on the Beer-Lambert law with information about the LAI and the NIR reflectance to correct for canopy structural effects. Finally, also soil moisture content and water included in surface minerals have to be considered. Both can influence the retrieved liquid water path over bare soil since the Beer-Lambert law is not able to distinguish between water included in different kinds of surface. An illustration can be found in Figure 14 where bare soil pixels with a measured CWC of 0 gcm$^{-2}$ show retrieved values of 0.05-0.08 gcm$^{-2}$.

Hunt et al. (2013) proposed not to use the absolute CWC values retrieved by the surface model based on the Beer-Lambert for further analyses. They pointed to alternative retrieval methods, which are insensitive to volume scattering effects, e.g., partial least squares regression (Asner and Martin, 2008; Li et al., 2008) or wavelet transforms (Cheng et al., 2011). However, our

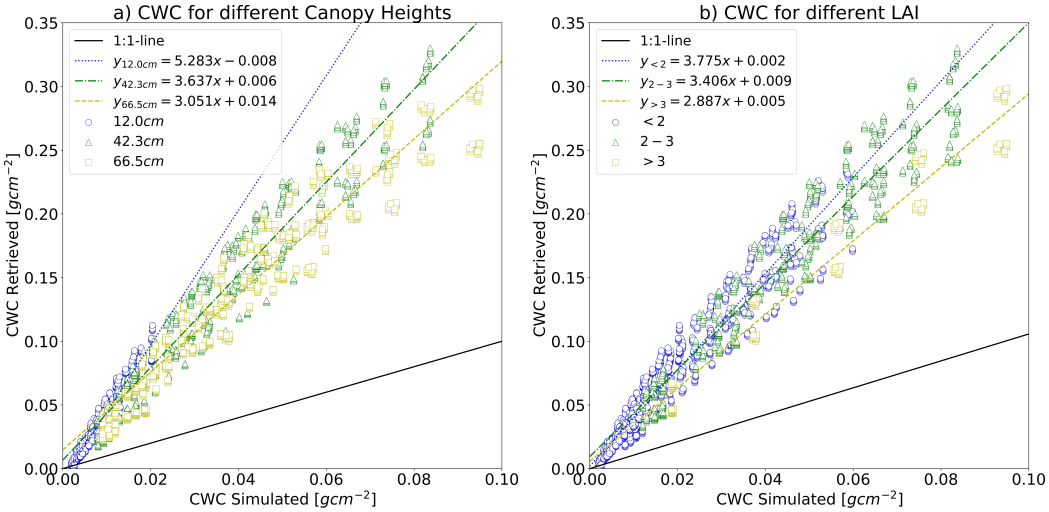


Figure 15: Comparison of retrieved CWC with simulated CWC as a function of a) mean canopy height, and b) LAI, from the simulated EnMAP data.

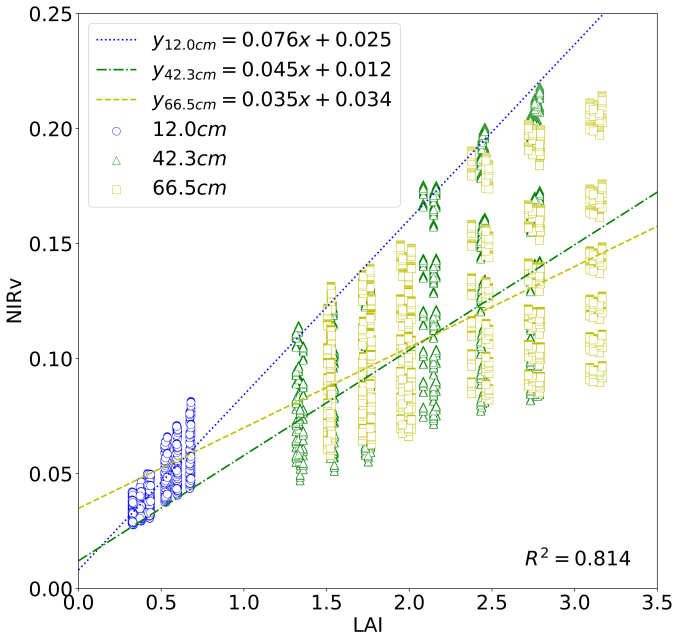


Figure 16: Comparison of NIRv with LAI for different mean canopy heights.

study shows that the Beer-Lambert surface reflectance model indeed can be improved with additional terms, but nevertheless, leads to promising results, which are already interpretable regarding absolute retrieved CWC.

## 5. Conclusion

We present a coupled retrieval of the three phases of water applied to spaceborne imaging spectroscopy measurements such as the upcoming German EnMAP mission. We analyze the sensitivity of the algorithm by a novel combination of field validation using CHRIS-PROBA measurements and a simulation study based on synthetic EnMAP data. The latter are obtained from canopy reflectance spectra simulated by the 3-dimensional HySimCaR system. Previous studies mainly validated their results by a visual interpretation (see Green et al. (2006), Thompson et al. (2015)) or used 1-dimensional PROSAIL spectra as input without simulating the atmosphere (see Clevers et al. (2010), Wocher et al. (2018)). Focusing on canopies of cereal crops, our sensitivity analysis demonstrates the ability of the proposed three phases of water retrieval to infer CWV and CWC with a high correlation to the simulation input showing an $R^2$ of 0.99 and 0.96, respectively.

However, our investigation shows that CWC is strongly overestimated by a mean factor of 3.37, which results from a large dependency on canopy structure and crop type. From a physical perspective, volume scattering effects related to LAI are primarily responsible for the observed overestimation. Otherwise, increasing the LAI from less than 2 to more than 3 leads to a decrease of the regression slope from 3.77 to 2.88. This supports the assumption that plant structure also plays an essential role in the overestimation. The more that stalks and ears influence the radiation signal, the less is the retrieval accuracy. This hypothesis is supported by the validation of CWC retrieved from CHRIS-PROBA data with field measurements. The analysis indeed yields an $R^2$ of 0.80 but provides a separation of different crop types depending on their physical structure. This

is also visualized by a remarkable clustering in the scatter plot. Furthermore, by producing smoother and more plausible CWV maps we achieve an accuracy improvement of CWV retrieved from CHRIS-PROBA data instead from a band ratio retrieval in the presence of liquid water absorption. This indicates that the algorithm leads to improvements in atmospheric correction procedures.

As a confirmatory of previous studies, we additionally show results of the three phases retrieval applied to airborne AVIRIS-C data. Based on an evaluation of the derived CWC from a vegetated surface, we assume that imaging spectroscopy tracks changes in CWC better than multispectral indices, such as the NDWI. Furthermore, the snow/ice retrieval from AVIRIS-C data produces a good correlation with the NDSI with an $R^2$ of 0.94 illustrating the ability of the three phases retrieval to clearly distinguish between different quantities of ice. In fact, higher amounts are tracked better than by using the NDSI since it becomes saturated at a value of around 0.9.

In summary, our study shows that the presented surface reflectance model based on the Beer-Lambert law can indeed be improved with additional terms to account for physical processes such as volume scattering. Also, the retrieval accuracy could be increased by integrating, if available, a priori information about the type of vegetation and the structure of the canopy in the framework of optimal estimation. However, even without improvement, this process has delivered promising results, which are already interpretable regarding absolute retrieved CWC. Recently launched or upcoming spaceborne imaging spectroscopy missions like PRISMA or EnMAP will provide valuable input for a further validation of the three phases of water retrieval.

## Acknowledgments

This study is funded within the EnMAP scientific preparation program under the DLR Space Administration with resources from the German Federal Ministry for Economic Affairs and Energy (grant ID 59EE1923) and the Helmholtz Centre Potsdam GFZ German Research Centre for Geosciences.

## Declaration of competing interest

The authors declare that they have no known competing financial interests or personal relationships that could have appeared to influence the work reported in this paper.

## References

AERONET, 2019. AERONET Aerosol Optical Depth Data Display Interface - Version 3 Aerosol Optical Depth. https://aeronet.gsfc.nasa.gov/cgi-bin/data_display_aod_v3. Accessed: 05/27/2019.

Asner, G.P., Martin, R.E., 2008. Spectral and chemical analysis of tropical forests: scaling from leaf to canopy levels. Remote Sens. Environ. 112, 3958–3970.

Bach, H., Rast, M., Nieke, J., 2018. CHIME - the copernicus hyperspectral imaging mission.

Badgley, G., Field, C.B., Berry, J.A., 2017. Canopy near-infrared reflectance and terrestrial photosynthesis. Sci. Adv. 3. doi:10.1126/sciadv.1602244.

Barducci, A., Guzzi, D., Marcoionni, P., Pippi, I., 2004. Algorithm for the retrieval of columnar water vapor from hyperspectral remotely sensed data. Appl. Optics 43, 5552–5563.

Barducci, A., Guzzi, D., Marcoionni, P., Pippi, I., 2005. CHRIS-PROBA performance evaluation: Signal-to-noise ratio, instrument efficiency and data quality from acquisitions over san rossore (Italy) test site. Proc. of the 3rd ESA CHRIS/Proba Workshop, 21-23 March (ESA SP-593, June 2005) .

Berk, A., Anderson, G.P., Acharya, P.K., Hoke, M.L., Chetwynd, J.H., Bernstein, L.S., Shettle, E.P., Matthew, M.W., Adler-Golden, S.M., 2003. MODTRAN4 version 3 revision 1 user's manual. Technical Report. Air Force Research Laboratory. Hanscom Air Force Base, MA, USA.

Berk, A., Bernstein, L.S., Robertson, D.C., 1989. MODTRAN: a moderate resolution model for LOWTRAN7. Technical Report GL-TR-89-0122. Air Force Geophysics Laboratory. Hanscom Air Force Base, MA, USA.

Bernstein, L.S., Berk, A., Sundberg, R.L., 2007. Application of MODTRAN to extra-terrestrial planetary atmospheres. Technical Report. Spectral Sciences, Inc.. Burlington, MA, USA.

Born, M., Wolf, E., 1959. Principles of Optics. Elsevier, New York, USA.

Chandrasekhar, S., 1960. Radiative Transfer Theory. Dover Publications Inc., Mineola, N.Y., USA.

Cheng, T., Rivard, B., Sanchez-Azofeifa, A., 2011. Spectroscopic determination of leaf water content using continuous wavelet analysis. Remote Sens. Environ. 115, 659–670.

Clevers, J.G.P.W., Kooistra, L., Schaepman, M.E., 2010. Estimating canopy water content using hyperspectral remote sensing data. Int. J. Appl. Earth Obs. 12, 119–125. doi:10.1016/j.jag.2010.01.007.

Diedrich, H., 2016. Observation of Total Column Water Vapour. Ph.D. thesis. Freie Universitaet Berlin, Mathematisch-Naturwissenschaftliche Fakultaet.

Diedrich, H., Preusker, R., Lindstrot, R., Fischer, J., 2013. Quantification of uncertainties of water vapour column retrievals using future instruments. Atmos. Meas. Tech. 6, 359–370.

Gao, B.C., 1996. NDWI - a normalized difference water index for remote sensing of vegetation liquid water from space. Remote Sens. Environ. 58, 257–266. doi:10.1016/S0034-4257(96)00067-3.

Gao, B.C., Goetz, A.F.H., 1990. Column atmospheric water vapor and vegetation liquid water retrievals from airborne imaging spectrometer data. J. Geophys. Res. 95(D4), 3549–3564.

Gao, B.C., Goetz, A.F.H., 1995. Retrieval of equivalent water thickness and information related to biochemical components of vegetation canopies from AVIRIS data. Remote Sens. Environ. 52, 155–162.

Goetz, A.F.H., Vane, G., Salomon, J.E., Rock, B.N., 1985. Imaging spectroscopy for earth remote sensing. Science 228, 1147–1153.

Govaerts, Y.M., Wagner, S., Lattanzio, A., Watts, P., 2010. Joint retrieval of surface reflectance and aerosol optical depth from MSG/SEVIRI observations with an optimal estimation approach: 1. theory. J. Geophys. Res. 115, D02203. doi:10.1029/2009JD011779.

Green, R.O., Conel, J.E., Margolis, J., Bruegge, J.C., Hoover, L.G., 1991. An inversion algorithm for retrieval of atmospheric and leaf water absorption from AVIRIS radiance with compensation for atmospheric scattering. Third Airborne Visible/Infrared Imaging Spectrometer (AVIRIS) Workshop , 51–61.

Green, R.O., Eastwood, M.L., Sarture, C.M., Chrien, T.G., Aronsson, M., Chippendale, B.J., Faust, J.A., Pavri, B.E., Chovit, C.J., Solis, M., Olah, M.R., Williams, O., 1998. Imaging spectroscopy and the airborne visible/infrared imaging spectrometer (AVIRIS). Remote Sens. Environ. 65, 227–248. doi:10.1016/S0034-4257(98)0064-9.

Green, R.O., Painter, T.H., Roberts, D.A., Dozier, J., 2006. Measuring the expressed abundance of the three phases of water with an imaging spectrometer over melting snow. Water Resour. Res. 42, W10402.

Guanter, L., Alonso, L., Gomez-Chova, L., Moreno, J., 2008b. CHRIS/PROBA atmospheric correction module - algorithm theoretical basis document .

Guanter, L., Alonso, L., Moreno, J., 2005. A method for the surface reflectance retrieval from PROBA/CHRIS data over land: Application to ESA SPARC campaigns. IEEE T. Geosci. Remote 43, 2908–2917. doi:10.1109/TGRS.2005.857915.

Guanter, L., Gomez-Chova, L., Moreno, J., 2008a. Coupled retrieval of aerosol optical thickness, columnar water vapor and surface reflectance maps from ENVISAT/MERIS data over land. Remote Sens. Environ. 112, 2898–2913.

Guanter, L., Kaufmann, H., Segl, K., Foerster, S., Rogass, C., Chabrillat, S., Kuester, T., Hollstein, A., Rossner, G., Chlebek, C., Straif, C., Fischer, S., Schrader, S., Storch, T., Heiden, U., Mueller, A., Bachmann, M., Muehle,

H., Mueller, R., Habermeyer, M., Ohndorf, A., Hill, J., Buddenbaum, H., Hostert, P., van der Linden, S., Leitao, P.J., Rabe, A., Doerffer, R., Krasemann, H., Xi, H., Mauser, W., Hank, T., Locherer, M., Rast, M., Staenz, K., Sang, B., 2015. The EnMAP spaceborne imaging spectroscopy mission for earth observation. Remote Sens. 7, 8830–8857. doi:10.3390/rs70708830.

Guanter, L., Richter, R., Kaufmann, H., 2009. On the application of the MODTRAN4 atmospheric radiative transfer code to optical remote sensing. Int. J. Remote Sens. 30, 1407–1424.

Hall, D.K., Riggs, G.A., Salomonson, V.V., 1995. Development of methods for mapping global snow cover using moderate resolution imaging spectroradiometer data. Remote Sens. Environ. 54, 127–140.

Hunt, E.R., Ustin, S.L., Riano, D., 2013. Satellite-based applications on climate change. Springer. chapter Remote sensing of leaf, canopy, and vegetation water contents for satellite environmental data records. pp. 335–357. doi:10.1007/978-94-007-5872-8_20.

Jacquemoud, S., Baret, F., 1990. PROSPECT: a model of leaf optical properties spectra. Remote Sens. Environ. 34, 75–91.

Jacquemoud, S., Baret, F., 1992. Crop structure and light microclimate: characterization and applications. Editions de l'INRA. chapter Estimating vegetation biophysical parameters by inversion of a reflectance model on high spectral resolution data. pp. 339–350.

Jacquemoud, S., Verhoef, W., Baret, F., Bacour, C., Zarco-Tejada, P.J., Asner, G.P., François, C., Ustin, S.L., 2009. PROSPECT + SAIL models: A review of use for vegetation characterization. Remote Sens. Environ. 113, S56–S66. Imaging Spectroscopy Special Issue.

Kedenburg, S., Vieweg, M., Gissibl, T., Giessen, H., 2012. Linear refractive index and absorption measurements of nonlinear optical liquids in the visible and near-infrared spectral region. Opt. Mater. Express 2, 1588–1611.

Kou, L., Labrie, D., Chylek, P., 1993. Refractive indices of water and ice in the 0.65- to 2.5-$\mu m$ spectral range. Appl. Opt. 32, 3531–3540.

Kuester, T., 2011. Modellierung von Getreidebestandsspektren zur Korrektur BRDF-bedingter Einfluesse auf Vegetationsindizes im Rahmen der EnMAP-Mission. Ph.D. thesis. Humboldt-Universitaet zu Berlin, Mathematisch-Naturwissenschaftliche Fakultaet II.

Kuester, T., Foerster, S., Chabrillat, S., Spengler, D., Guanter, L., 2017. Assessing the influence of variable fractional vegetation cover on soil spectral features using simulated canopy reflectance modeling, in: 10th EARSeL SIG Imaging Spectroscopy Workshop, Zurich, Switzerland, Zurich, Switzerland.

Kuester, T., Spengler, D., 2018. Structural and spectral analysis of cereal canopy reflectance and reflectance anisotropy. Remote Sens. 10. doi:10.3390/rs10111767.

Kuester, T., Spengler, D., Barczi, J.F., Segl, K., Hostert, P., Kaufmann, H., 2014. Modeling multitemporal and hyperspectral vegetation canopy bidirectional reflectance using detailed virtual 3D canopy models. IEEE T. Geosci. Remote 4, 2096–2108.

Lee, C.M., Cable, M.L., Hook, S.J., Green, R.O., Ustin, S.L., Mandl, D.J., Middleton, E.M., 2015. An introduction to the NASA Hyperspectral InfraRed Imager (HyspIRI) mission and preparatory activities. Remote Sens. Environ. 167, 6–19. doi:10.1016/j.rse.2015.06.012.

Lewis, P., 1999. Three-dimensional plant modeling for remote sensing simulation studies using the botanical plant modeling system. Agronomie 19, 185–210.

Li, L., Cheng, Y.B., Ustin, S.L., Hua, X.T., Riano, D., 2008. Retrieval of vegetation equivalent water thickness from reflectance using genetic algorithm (GA)-partial least squares (PLS) regression. Adv. Space Res. 41, 1755–1763.

Loizzo, R., Guarini, R., Longo, F., Scopa, T., Formaro, R., Facchinetti, C., Varacalli, G., 2018. PRISMA: The Italian hyperspectral mission. Proc. IGARSS .

Meier, U., 1997. Growth stages of mono- and dicotyledonous plants: BBCH-Monograph. Blackwell Wissenschafts-Verlag.

Mueller, R., Avbelj, J., Carmona, E., Eckhardt, A., Gerasch, B., Graham, L., Guenther, B., Heiden, U., Ickers, J., Kerr, G., Knodt, U., Krutz, D., Krawczyk, H., Makarau, A., Miller, R., Perkins, R., Walter, I., 2016. The new hyperspectral sensor DESIS on the multi-payload platform MUSES installed on the ISS. Int. Arch. Photogramm. 41, 461–467. doi:10.5194/isprsarchives-XLI-B1-461-2016.

Nicodemus, F.E., Richmond, J.C., Hsia, J.J., Ginsberg, I.W., Limperis, T., 1977. Geometrical Considerations and Nomenclature for Reflectance. Technical Report. National Bureau of Standards, Washington, D.C. 20234.

Pasqualotto, N., Delegido, J., Wittenberghe, S.V., Verrelst, J., Rivera, J.P., Moreno, J., 2018. Retrieval of canopy water content of different crop types with two new hyperspectral indices: Water Absorption Area Index and Depth Water Index. Int. J. Appl. Earth Obs. Geoinformation 67, 69–78. doi:10.1016/j.jag.2018.01.002.

Petty, G.W., 2004. A First Course in Atmospheric Radiation. 1. ed., Sundog Publishing, Madison, WI, USA.

Riggs, G.A., Hall, D.K., 2015. MODIS snow products collection 6 user guide. Technical Report.

Roberts, D., Brown, K., Green, R., Ustin, S., Hinckley, T., 1998. Investigating the relationship between liquid water and leaf area in clonal populus. Summaries of the Seventh JPL Airborne Earth Science Workshop January 12-16, 1998 1, 335–344.

Rodgers, C.D., 2000. Inverse Methods for Atmospheric Sounding: Theory and Practice. World Scientific Pub Co., Oxford, UK.

Rothman, L.S., Gordon, I.E., Barbe, A., Brenner, D.C., Bernath, P.F., Birk, M., Boudon, V., Brown, L.R., Campargue, A., Champion, J.P., Chance, K., Coudert, L.H., Diana, V., Devi, V.M., Fally, S., Flaud, J.M., Gamache, R.R., Goldman, A., Jacquemart, D., Kleiner, I., Lacome, N., Lafferty, W.J., Mandin, J.Y., Massie, S.T., Mikhailenko, S.N., Miller, C.E., Moazzen-Ahmadi, N., Naumenko, O.V., Nikitin, A.V., Orphal, J., Perevalov, V.I., Perrin, A., Predoi-Cross, A., Rinsland, C.P., Rotger, M., Simeckova, M., Smith, M.A.H., Sung, K., Tashkun, S.A., Tennyson, J., Toth, R.A., Vandaele, A.C., Auwera, J.V., 2009. The HITRAN 2008 molecular spectroscopic database. J. Quant. Spectrosc. Ra. 110, 533–572. doi:DOI: 10.1016/j.jqsrt.2009.02.013.

Schaepman, M.E., Ustin, S.L., Plaza, A.J., Painter, T.H., Verrelst, J., Liang, S., 2009. Earth system science related imaging spectroscopy - an assessment. Remote Sens. Environ. 113, S123–S137. doi:10.1016/j.rse.2009.03.001.

Segl, K., Kuester, T., Rogass, C., Kaufmann, H., Sang, B., Hofer, S., 2012. EeteS - the EnMAP End-to-End Simulation Tool. IEEE J. Sel. Top. Appl. 5, 522–530. doi:10.1109/JSTARS.2012.2188994.

Spengler, D., 2014. Charakterisierung von Getreidearten aus hyperspektralen Fernerkundungsdaten auf der Basis von 4D-Bestandsmodellen. Ph.D. thesis. Technische Universitaet Berlin, Fakultaet VI - Planen Bauen Umwelt.

Spengler, D., Frick, A., Davey, C., Peisker, T., Kaufmann, H., 2011. Estimation of surface soil moisture content using imaging spectroscopy - a simulation case study, in: 7th EARSeL SIG Imaging Spectroscopy Workshop, Edinburgh, Scotland, United Kingdom.

Spengler, D., Kuester, T., Frick, A., Scheffler, D., Kaufmann, H., 2013. Correcting the influence of vegetation on surface soil moisture indices by using hyperspectral artificial 3D-canopy models, in: Proceedings SPIE, Dresden, Germany, p. 9. doi:10.1117/12.2028496.

Stamnes, K., Tsay, S.C., Wiscombe, W., Jayaweera, K., 1988. A numerically stable algorithm for discrete ordinates method radiative transfer in multiple scattering and emitting layered media. Appl. Optics 27, 2502–2509.

Thompson, D.R., Gao, B.C., Green, R.O., Roberts, D.A., Dennison, P.E., Lundeen, S.R., 2015. Atmospheric correction for global mapping spectroscopy: ATREM advances for the HyspIRI preparatory campaign. Remote Sens. Environ. 167, 64–77. doi:10.1016/j.rse.2015.02.010.

Thompson, D.R., McCubbin, I., Gao, B.C., Green, R.O., Matthews, A.A., Mei, F., Meyer, K.G., Platnick, S., Schmid, B., Tomlinson, J., Wilcox, E., 2016. Measuring cloud thermodynamic phase with shortwave infrared imaging spectroscopy. J. Geophys. Res.-Atmos. 121, 9174–9190. doi:10.1002/2016JD024999.

Thompson, D.R., Natraj, V., Green, R.O., Helmlinger, M.C., Gao, B.C., Eastwood, M.L., 2018. Optimal estimation for imaging spectrometer atmospheric correction. Remote Sens. Environ. 216, 355–373. doi:10.1016/j.rse.2018.07.003.

van der Tol, C., Verhoef, W., Timmermans, J., Verhoef, A., Su, Z., 2009. An integrated model of soil-canopy spectral radiances, photosynthesis, fluorescence, temperature and energy balance. Biogeosciences 6, 3109–3129.

Vane, G., Goetz, A.F.H., 1988. Terrestrial imaging spectroscopy for earth remote sensing. Remote Sens. Environ. 24, 1–29.

Vane, G., Green, R.O., Chrien, T.G., Enmark, H.T., Hansen, E.G., Porter, W.M., 1993. The airborne visible/infrared imaging spectrometer (AVIRIS). Remote Sens. Environ. 44, 127 – 143. doi:10.1016/S0034-4257(93)90012-M.

Wagner, S.C., Govaerts, Y.M., Lattanzio, A., 2010. Joint retrieval of surface reflectance and aerosol optical depth from MSG/SEVIRI observations with an optimal estimation approach: 2. implementation and evaluation. J. Geophys.

Res. 115, D02204. doi:10.1029/2009JD011780.

Warren, S.G., 1984. Optical constants of ice from the ultraviolet to the microwave. Appl. Optics 23, 1206–1225. doi:10.1364/AO.23.001206.

Widlowski, J.L., Taberner, M., Pinty, B., Bruniquel-Pinel, V., Disney, M., Fernades, R., Gastellu-Etchegorry, J.P., Gobron, N., Kuusk, A., Lavergne, T., Leblanc, S., Lewis, P., Martin, E., Ottus, M.M., North, P.R.J., Qin, W., Robustelli, M., Rochdi, N., Ruiloba, R., Soler, C., Thompson, R., Verhoef, W., Verstraete, M.M., Xie, D., 2007. The third RAdiation transfer Model Intercomparison (RAMI) exercise: Documenting progress in canopy reflectance models. J. Geophys. Res. 112, 28.

Wocher, M., Berger, K., Danner, M., Mauser, W., Hank, T., 2018. Physically-bases retrieval of canopy equivalent water thickness using hyperspectral data. Remote Sens. 10, 1924–1940. doi:10.3390/rs10121924.

Xiao, Y., Zhao, W., Zhou, D., Gong, H., 2014. Sensitivity analysis of vegetation reflectance to biochemical and biophysical variables at leaf, canopy, and regional scales. IEEE T. Geosci. Remote 52, 4014–4024. doi:10.1109/TGRS.2013.2278838.

Zhang, Q.X., Li, Q.B., Zhang, G.J., 2011. Scattering impact analysis and correction for leaf biochemical parameter estimation using VIS-NIR spectroscopy. Spectroscopy 26, 28–39.